Observational constraints on tidal effects using orbital eccentricities

Nawal Husnoo, Frédéric Pont, Tsevi Mazeh, Daniel Fabrycky, Guillaume Hébrard, François Bouchy, Avi Shporer

Monthly Notices
of the
ROYAL ASTRONOMICAL SOCIETY

Mon. Not. R. Astron. Soc. **422,** 3151–3177 (2012) doi:10.1111/j.1365-2966.2012.20839.x

Observational constraints on tidal effects using orbital eccentricities★

Nawal Husnoo,[1]† Frédéric Pont,[1] Tsevi Mazeh,[2] Daniel Fabrycky,[3] Guillaume Hébrard,[4,5] François Bouchy[4,5] and Avi Shporer[6]

[1]*School of Physics, University of Exeter, Exeter EX4 4QL*
[2]*School of Physics and Astronomy, Tel Aviv University, Tel Aviv 69978, Israel*
[3]*Harvard–Smithsonian Center for Astrophysics, 60 Garden Street, Cambridge, MA 02138, USA*
[4]*Institut d'Astrophysique de Paris, UMR7095 CNRS, Université Pierre & Marie Curie, 98bis boulevard Arago, 75014 Paris, France*
[5]*Observatoire de Haute-Provence, CNRS/OAMP, 04870 Saint-Michel-l'Observatoire, France*
[6]*Las Cumbres Observatory Global Telescope Network, 6740 Cortona Drive, suite 102, Goleta, CA 93117, USA*

Accepted 2012 February 28. Received 2012 February 24; in original form 2011 September 14

ABSTRACT

We have analysed radial velocity measurements for known transiting exoplanets to study the empirical signature of tidal orbital evolution for close-in planets. Compared to standard eccentricity determination, our approach is modified to focus on the rejection of the null hypothesis of a circular orbit. We are using a Markov Chain Monte Carlo analysis of radial velocity measurements and photometric constraints, including a component of correlated noise, as well as Bayesian model selection to check if the data justify the additional complexity of an eccentric orbit. We find that among planets with non-zero eccentricity values quoted in the literature, there is no evidence for an eccentricity detection for the seven planets CoRoT-5b, WASP-5b, WASP-6b, WASP-10b, WASP-12b, WASP-17b and WASP-18b. In contrast, we confirm the eccentricity of HAT-P-16b, $e = 0.034 \pm 0.003$, the smallest eccentricity that is reliably measured so far for an exoplanet as well as that of WASP-14b, which is the planet at the shortest period ($P = 2.24$ d), with a confirmed eccentricity, $e = 0.088 \pm 0.003$. As part of the study, we present new radial velocity data using the HARPS spectrograph for CoRoT-1, CoRoT-3, WASP-2, WASP-4, WASP-5 and WASP-7 as well as the SOPHIE spectrograph for HAT-P-4, HAT-P-7, TrES-2 and XO-2.

We show that the dissipative effect of tides raised in the planet by the star and vice versa explain all the eccentricity and spin–orbit alignment measurements available for transiting planets. We revisit the mass–period relation and consider its relation to the stopping mechanism of orbital migration for hot Jupiters. In addition to CoRoT-2 and HD 189733, we find evidence for excess rotation of the star in the systems CoRoT-18, HAT-P-20, WASP-19 and WASP-43.

Key words: planetary systems.

1 INTRODUCTION

Most of the information we have about the formation, evolution and structure of exoplanets have come from the study of transiting planets. This is possible because the combination of radial velocity (RV) measurements with transit photometry can provide powerful constraints on the physical and orbital parameters of an exoplanet, such as the planetary mass, radius, orbital eccentricity, etc.

A selection effect due to geometry means that most transiting planets with RV confirmation are found on very short period orbits with $P \sim 1$–20 d. The close-in planets with periods of a few days are expected to experience strong tidal effects (e.g. Rasio & Ford 1996), which should increase sharply with decreasing period and these orbits are thus expected to circularize on a time-scale much smaller than the system age. A higher tendency for such circular orbits is indeed observed in the sample of transiting planets, as compared to those from RV surveys. This has been interpreted as a signature for tidal circularization. The transition from eccentric orbits to circular orbits at short period has also been seen in binary star systems (e.g. Mathieu & Mazeh 1988; Mazeh 2008). Over the last few years, we have carried out a monitoring programme to obtain several RV measurements of known transiting planetary systems with the intention of refining the orbital properties such as orbital eccentricity and spin–orbit alignment angle. We have used the SOPHIE spectrograph in the Northern hemisphere and

★Based on observations made at the 1.93-m telescopes at Observatoire de Haute-Provence (CNRS), France, with the SOPHIE spectrograph.
†E-mail: nawal@astro.ex.ac.uk

the HARPS spectrograph in the Southern hemisphere (e.g. Hébrard et al. 2008; Loeillet et al. 2008; Husnoo et al. 2011; Pont et al. 2011, ESO Prog. 0812.C-0312).

One issue is the difficulty of measuring the orbital eccentricity of exoplanets for faint stars, especially for low-mass planets. While it is impossible to prove that an orbit is circular, with $e = 0$ exactly, we can place an upper limit on the eccentricity of a given orbit (e.g. reject $e > 0.1$ at the 95 per cent confidence level). In fact, a number of eccentric orbits have been detected at short period, but follow-up observations using photometry or additional RV measurements led to the conclusion that some of these eccentricities had originally been overestimated. For example, the WASP-10 system (Christian et al. 2009) was revisited by Maciejewski et al. (2011b), who showed that the initially reported eccentricity ($e = 0.059^{+0.014}_{-0.004}$) had been overestimated and was in fact compatible with zero. The orbital eccentricity of WASP-12b (Hebb et al. 2009, $e = 0.049 \pm 0.015$) is similarly compatible with zero (Husnoo et al. 2011), and the original detection was possibly due to systematic effects (weather conditions, instrumental drifts, stellar spots or scattered sunlight).

The eccentricity distribution at short period has a crucial importance for any theory of planetary formation and orbital evolution. Planets on orbits that are consistent with circular gather in a well-defined region of the mass–period plane, close to the minimum period for any given mass (Pont et al. 2011). We now show that there are no exceptions to this pattern, and revisit some apparent exceptions as reported in the literature. As an ensemble, the totality of transiting planets considered in this study is in agreement with classical tide theory, with orbital circularization due to tides raised on the planet by the star and tides on the star raised by the planet, to varying degree depending on the position of the planet–star system in the mass–period plane.

In this study, we consider new RV measurements made with HARPS and SOPHIE, as well as measurements present in the literature. We use photometric constraints in the form of the orbital period P and mid-transit time $T_{\rm tr}$, both of which can be measured accurately using transit photometry, and we also consider constraints from the secondary eclipse where available. In fact, if we define the orbital phase $\phi = (t - T_0)/P$ to be zero at mid-transit time $T_0 = T_{\rm tr}$, a planet on a circular orbit would have a mid-occultation phase of $\phi = 0.5$ (by symmetry). A planet that is on an eccentric orbit will, however, have a mid-occultation phase different from 0.5 (unless the orbital apsides are aligned along the line of sight). This allows us to place a constraint on the $e\cos\omega$ projection of the eccentricity, as given by Winn et al. (2005) (slightly modified):

$$e\cos\omega \simeq \frac{\pi}{2}\left(\phi_{\rm occ} - 0.5\right), \tag{1}$$

to first order in e, where we now define $\phi_{\rm occ}$ to be the phase difference between the mid-transit time and the mid-occultation time, i.e. $\phi_{\rm occ} = (T_{\rm sec} - T_{\rm tr})/P$, where $T_{\rm sec}$ is the time of the secondary eclipse following the transit time $T_{\rm tr}$. The component $e\sin\omega$ is dependent on a ratio involving the durations of the occultation and transit (Winn et al. 2005),

$$e\sin\omega \simeq \frac{T_{\rm tra} - T_{\rm occ}}{T_{\rm tra} + T_{\rm occ}}, \tag{2}$$

to first order in e, where $T_{\rm tra}$ and $T_{\rm occ}$ are the transit and occultation durations, respectively, although this constraint is weaker than the one on $e\cos\omega$.

In addition to the reanalysis of RV measurements with photometric constraints, we also introduce two modifications to the Markov Chain Monte Carlo (MCMC) process commonly used by teams analysing RV data to work out the orbital parameters of transiting exoplanets. This involves a new treatment of the correlated noise present in most RV data sets, as well as analysing the data in model selection mode to check if an eccentric orbit is indeed justified, given the additional complexity of the eccentric version of a Keplerian orbit.

The present time is significant in the study of exoplanets, because a number of high quality measurements are now available for the three main observable effects of tides: circularization, synchronization and spin–orbit alignment. In Section 2, we describe our new RV measurements obtained with SOPHIE and HARPS for 10 objects, as well as the measurements we collected from the literature for this study. We then describe the analysis we performed in Section 3. In Section 4, we describe the objects in the classes 'eccentric', 'compatible with circular, $e < 0.1$', and 'poorly constrained' and present the updated eccentricities, as shown in Table 19. In Section 5, we consider our orbital eccentricity estimates in the light of tidal effects inside the planet due to the star and vice versa. We find that our results are compatible with classical tidal theory, removing the need for perturbing stellar or planetary companions to excite non-negligible eccentricities in short period orbits.

Winn et al. (2010) presented a discussion on the available measurements of the projected spin–orbit alignment angles, and found that hot planet-hosting stars ($T_{\rm eff} > 6250$ K) had random obliquities whereas cooler stars ($T_{\rm eff} < 6250$ K) tended to have aligned rotations. These authors suggested that this dichotomy can be explained if all these stars harbouring a planetary system start off with a random obliquity following some dynamical interaction, but only cool stars with a significant convective layer are able to undergo tidal effects leading to alignment. We verify in Section 5 that the strong exceptions WASP-8 and HD 80606 are indeed systems with weak tidal interactions, and that the observation that these two are misaligned is not incompatible with tidal theory.

In a number of cases, such as HD 189733 (Henry & Winn 2008), WASP-19 (Hebb et al. 2010) and CoRoT-2 (Lanza et al. 2009), the rotational period of the star is known from photometric monitoring. Assuming the results of Winn et al. (2010) are correct in the sense that the convective layer in G dwarfs would cause tidal dissipation that aligns the stellar equator with the planetary orbit, the negligible value of the projected spin–orbit angle λ means that the obliquity is indeed zero, i.e. the stellar equators are aligned with the orbital planes. In this case, a measurement of the projected equatorial rotational velocity of the star ($v\sin i$) through Doppler broadening yields the rotational period of the star. This means that for G dwarfs at least, we have enough information to observe the effect of tidal interactions on the stellar rotation. We show in Section 5 that in addition to CoRoT-2 and HD 189733 (Pont et al. 2009), we find evidence for excess rotation of the star in the systems CoRoT-18, HAT-P-20, WASP-19 and WASP-43.

The preliminary results from this study were published in Pont et al. (2011), and the exact numerical values of the eccentricities have been updated in this paper to reflect our new choice of RV measurement correlation time-scale $\tau = 1.5$ d (see Section 3.2), as opposed to $\tau = 0.1$ d in Pont et al. (2011). The overall results, i.e. the clear separation between orbits that are consistent with circular and eccentric orbits in the mass–period plane, does not change in this paper. The mass–period relation of Mazeh et al. (2005) is still clearly present, with low-mass hot Jupiters on orbits that are consistent with circular clumping in a definite region of the mass–period plane, with heavier objects moving closer in, to shorter periods. This strongly suggests that tidal effects are involved in the stopping mechanism of these objects. A similar stopping mechanism can be seen at higher planetary masses, but destruction of the planet

is not excluded in many cases. Other effects, such as spin–orbit alignment and stellar spin-up, also point strongly towards the scenario of Rasio & Ford (1996) where the short period orbits of hot Jupiters are formed by dynamical scattering, which produces eccentric and misaligned orbits. This is followed by tidal dissipation which leads to circularization at short period, spin–orbit alignment and synchronization of the rotation of the host star.

2 OBSERVATIONS

We include 73 measurements for six objects with the HARPS spectrograph (Tables 1–6) and 45 measurements for four objects with the SOPHIE spectrograph (Tables 7–10). Both are bench-mounted, fibre-fed spectrograph built on the same design principles and their thermal environments are carefully controlled, to achieve precise RV measurements. The two instruments have participated in the detection and characterization of numerous transiting exoplanets, notably from the WASP and CoRoT transit searches. The wavelength-calibrated high-resolution spectra from the instruments are analysed using a cross-correlation technique which compares them with a mask consisting of theoretical positions and widths of the stellar absorption lines at zero velocity (Pepe et al. 2002).

We carried out a literature survey and collected RV measurements for 54 transiting planets, as well as other relevant data such as the orbital periods and the time of mid-transit. For the cases of CoRoT-1, CoRoT-2 and GJ-436, we also used the secondary eclipse constraint on the eccentricity component $e \cos \omega$ from Alonso et al. (2009a,b) and Deming et al. (2007), respectively.

Table 1. HARPS RV measurements for CoRoT-1 (errors include random component only).

Time (BJD-245 0000)	RV (km s^{-1})	σ_{RV} (km s^{-1})
4385.86631	23.4168	0.0190
4386.83809	23.6726	0.0139
4387.80863	23.3155	0.0149
4419.81749	23.5811	0.0123
4420.80300	23.3290	0.0118
4421.81461	23.6586	0.0113
4446.77797	23.3936	0.0145
4447.75517	23.4562	0.0130
4448.77217	23.6982	0.0126
4479.67146	23.3161	0.0123
4480.65370	23.6836	0.0140
4481.63818	23.5129	0.0173
4525.59523	23.6451	0.0116
4529.56406	23.3324	0.0127
4530.58002	23.5743	0.0105
4549.58179	23.5793	0.0280
4553.49391	23.3652	0.0124
4554.57636	23.6696	0.0157
4768.77120	23.7041	0.0092
4769.76601	23.4802	0.0104
4770.80872	23.3613	0.0108
4771.76514	23.6955	0.0102
4772.76824	23.4379	0.0109
4773.76896	23.3980	0.0095

Table 2. HARPS RV measurements for CoRoT-3 (errors include random component only).

Time (BJD-245 0000)	RV (km s^{-1})	σ_{RV} (km s^{-1})
4768.52895	−56.5039	0.0036
4769.51404	−58.1970	0.0038
4770.51329	−56.1017	0.0046
4772.52655	−55.9171	0.0047
4773.52957	−58.2227	0.0042

Table 3. HARPS RV measurements for WASP-2 (errors include random component only).

Time (BJD-245 0000)	RV (km s^{-1})	σ_{RV} (km s^{-1})
4766.56990	−27.8402	0.0033
4767.52666	−27.6797	0.0023
4768.56373	−27.7842	0.0018
4769.54823	−27.7343	0.0017
4770.54665	−27.7131	0.0026
4771.54501	−27.8099	0.0031
4772.56012	−27.6489	0.0027
4773.56432	−27.8568	0.0019

Table 4. HARPS RV measurements for WASP-4 (errors include random component only).

Time (BJD-245 0000)	RV (km s^{-1})	σ_{RV} (km s^{-1})
4762.60256	57.6687	0.0028
4763.62220	57.5637	0.0022
4764.58386	57.9085	0.0035
4765.59031	57.9871	0.0038
4768.60378	57.9109	0.0022
4769.58081	57.9784	0.0023
4769.71186	58.0331	0.0017
4770.58784	57.6591	0.0024
4770.72474	57.7930	0.0023
4771.57892	57.6311	0.0021
4771.68481	57.5752	0.0019
4772.59125	57.9518	0.0025
4773.59429	57.9811	0.0018
4773.70377	58.0346	0.0024

Table 5. HARPS RV measurements for WASP-5 (errors include random component only).

Time (BJD-245 0000)	RV (km s^{-1})	σ_{RV} (km s^{-1})
4768.63152	19.7967	0.0022
4768.73169	19.8696	0.0018
4769.62838	20.1047	0.0023
4770.62473	20.1231	0.0022
4770.76117	20.2255	0.0031
4771.60846	19.7737	0.0017
4771.71520	19.7446	0.0021
4772.63762	20.2588	0.0023
4772.73505	20.2071	0.0022
4773.62311	19.8540	0.0021
4773.73277	19.9582	0.0025

Table 6. HARPS RV measurements for WASP-7 (errors include random component only).

Time (BJD-245 0000)	RV (km s^{-1})	σ_{RV} (km s^{-1})
4762.53711	−29.4388	0.0024
4763.57798	−29.4994	0.0023
4764.50127	−29.5469	0.0032
4765.54456	−29.3948	0.0032
4767.54077	−29.3485	0.0031
4768.57924	−29.5636	0.0021
4769.64528	−29.5332	0.0018
4770.64161	−29.4468	0.0022
4771.62297	−29.3421	0.0019
4772.65474	−29.4212	0.0022
4773.63924	−29.5829	0.0020

Table 7. SOPHIE RV measurements for HAT-P-4 (uncertainties include random component only).

Time (BJD-245 0000)	RV (km s^{-1})	σ_{RV} (km s^{-1})
5003.41234	−1.3253	0.0206
5005.47636	−1.3669	0.0122
5006.50185	−1.3244	0.0123
5007.42327	−1.4822	0.0129
5008.39084	−1.4143	0.0131
5009.38832	−1.3465	0.0132
5010.39331	−1.4711	0.0131
5011.42884	−1.4181	0.0129
5012.46735	−1.3504	0.0131
5013.45923	−1.4487	0.0128
5014.43881	−1.4106	0.0123
5015.48148	−1.3212	0.0124
5016.41444	−1.4666	0.0119

Table 8. SOPHIE RV measurements for HAT-P-7 (uncertainties include random component only).

Time (BJD-245 0000)	RV (km s^{-1})	σ_{RV} (km s^{-1})
5002.48517	−10.2995	0.0100
5003.52118	−10.6910	0.0103
5004.59910	−10.2681	0.0137
5005.49926	−10.6377	0.0101
5006.55335	−10.2564	0.0101
5007.53107	−10.5975	0.0101
5008.47624	−10.4027	0.0106
5010.43095	−10.5681	0.0102
5011.52259	−10.3835	0.0102
5013.60648	−10.3090	0.0093
5014.57426	−10.6862	0.0101
5015.58518	−10.2680	0.0103
5016.54123	−10.6808	0.0084

Given the rapid rate of announcement of new transiting exoplanets, we had to stop the clock somewhere, and we picked the 2010 July 1. We selected only objects that had been reported in peer-reviewed journals or on the online preprint archive (ArXiV.org).

Table 9. SOPHIE RV measurements for TrES-2 (uncertainties include random component only).

Time (BJD-245 0000)	RV (km s^{-1})	σ_{RV} (km s^{-1})
5005.57207	−0.4489	0.0107
5006.57091	−0.2231	0.0100
5007.57482	−0.2619	0.0105
5008.44948	−0.4742	0.0106
5010.44234	−0.4505	0.0107
5011.51233	−0.2499	0.0110
5013.59448	−0.4207	0.0114
5014.56301	−0.1604	0.0108
5015.57356	−0.5090	0.0107
5016.55442	−0.2197	0.0110

Table 10. SOPHIE RV measurements for XO-2 (uncertainties include random component only).

Time (BJD-245 0000)	RV (km s^{-1})	σ_{RV} (km s^{-1})
4878.41245	46.7905	0.0091
4879.38681	46.9667	0.0084
4886.39349	46.7748	0.0095
4887.44867	46.9583	0.0084
4888.47514	46.7722	0.0085
4889.40965	46.8778	0.0086
4890.46546	46.8994	0.0085
4893.41643	46.8202	0.0087
4894.44335	46.8073	0.0121

Moreover, we selected systems with well-measured parameters (planetary radius R_p and mass M_p to within 10 per cent) and excluded faint objects ($V > 15$). At that time, 64 such systems were known. We reanalyse the existing RV data for 54 transiting systems, providing additional RV measurements for 10 systems described above, and include 10 systems without further reanalysis of orbital ephemeris. In Section 4.5, we include a further 16 systems, most of which had been discovered in the mean time. The planets involved in this study are listed on the webpage http://www.inscience.ch/transits/, where we also include the parameters $v \sin i$ (the projected rotation velocity of the host star), P_{rot} (the orbital period of the host star) and the projected spin–orbit angle λ where available.

3 ANALYSIS

We used the RV data as well as the constraints on the orbital period P and mid-transit time T_{tr} (and $e \cos \omega$ where available) from photometry as described in Section 2. To calculate the median values of the derived parameters and their corresponding uncertainties, we marginalize over their joint probability distribution using an MCMC analysis with the Metropolis–Hastings algorithm. This has been described in the past by Holman et al. (2006) and our implementation is described in Pont et al. (2009). We model the RV using a Keplerian orbit and run the MCMC for 500 000 steps, the first 50 000 of which are then dropped to allow the MCMC to lose memory of the initial parameters. We verify that the autocorrelation length of each chain is much shorter than the chain length to ensure that the relevant region of parameter space is properly explored.

Although this procedure is common practice in the community, we bring two changes. The first is a modification to the merit function that is used to work out the likelihood of a set of parameters given the data, to include the effects of correlated noise. This is described in Section 3.1. The second modification we bring is that we not only consider the case of an orbital model with a free eccentricity e, but also work out the likelihood for a circular orbit (i.e. with e fixed at zero). We then compare the two models by including a penalty for the additional complexity in the eccentric one (i.e. 2 additional degrees of freedom). We do this by using the Bayesian Information Criterion (BIC), as described in Section 3.3.

We report the median value in the chain for each parameter, as well as the central 68.4 per cent confidence interval on the parameter. A circular orbit model for an orbit that is in fact eccentric would artificially make the uncertainties in the derived parameters smaller, so in the case of the systemic velocity V_0 and the semi-amplitude K, we report the median values from a circular orbit model, yet we include the confidence intervals derived from the eccentric model.

3.1 The treatment of correlated noise

Correlated noise can be important in the analysis of transit light curves (Pont, Zucker & Queloz 2006), and we included this in the analysis of RV measurements in the case of WASP-12 (see Husnoo et al. 2011). If we assume uncorrelated Gaussian noise when analysing data that are affected by correlated noise, we run the risk of overestimating the importance of a series of measurements that were obtained in quick succession, and this can have implications, for example, in estimating the orbital eccentricity.

From Sivia (2006), the likelihood function for some data, given a model, is given by

$$\mathrm{P}(\boldsymbol{D}|\boldsymbol{\theta}, I) = \frac{\exp\left[-\frac{1}{2}(\boldsymbol{F}-\boldsymbol{D})^{\mathrm{T}}\boldsymbol{C}^{-1}(\boldsymbol{F}-\boldsymbol{D})\right]}{\sqrt{(2\pi)^N \det(\boldsymbol{C})}}, \tag{3}$$

where $\boldsymbol{D}$ is the RV time series data expressed as a vector, $\boldsymbol{\theta}$ is the vector of model parameters and $\boldsymbol{F}$ is the predicted values from the Keplerian model. In this case, χ^2 is defined by

$$\chi^2 = (\boldsymbol{F}-\boldsymbol{D})^{\mathrm{T}}\boldsymbol{C}^{-1}(\boldsymbol{F}-\boldsymbol{D}), \tag{4}$$

where $\boldsymbol{C}$ is the covariance matrix, which remains constant throughout the MCMC analysis for each system. In the case of independent measurements, the components of the covariance matrix $\boldsymbol{C}$ would be obtained using

$$C_{k,k'} = \begin{cases} \sigma_k^2 & \text{for } k = k' \\ 0 & \text{otherwise,} \end{cases} \tag{5}$$

whereas in the presence of some correlated noise, we modify this to include a squared exponential covariance kernel so that

$$C_{k,k'} = \delta_{k,k'}\sigma_k^2 + \sum_{i=1}^{M} \sigma_i^2 \exp -\frac{(t_k - t_{k'})^2}{2\tau_i^2}, \tag{6}$$

where σ_k is the formal uncertainty on each measurement k as obtained from the data reduction for that measurement, and the sum over M terms having the form $\sigma_i^2 \exp -\frac{(t_k - t_{k'})^2}{2\tau_i^2}$ allows us to include a number of stationary covariance functions to account for correlations in the noise, occurring over the time-scales of hours to days.

In practice, it can be tricky to estimate the values of τ_i and σ_i for RV data sets, especially where the number of measurements is few or the phase coverage is incomplete. Given the small data sets, we elect to use a single time-invariant correlation term, setting $M = 1$. The time-scale is now called τ, and the corresponding value of σ_i is now called σ_{r}, where the subscript r indicates 'red noise' (Pont et al. 2006). A fully Bayesian analysis would require that we assign priors to these two parameters and then marginalize over them. In practice, the sparse sampling and small data sets for RV observations mean that it is very difficult to perform Bayesian marginalization over these two parameters, and the results would depend on the prior space chosen (e.g. τ, $\log\tau$, etc.). We therefore use a single pair of parameters for τ and σ_{r}. Using a single term in the sum in equation (6) makes the expression less flexible, but prior experience shows that correlations over the $\sim$1 d time-scale are particularly important for RV data sets, especially for measurements taken in the same night (see e.g. Husnoo et al. 2011, for the case of WASP-12). For data sets where the reduced χ^2 for a given model (circular or eccentric) was larger than unity, we estimated σ_{r} by repeating the MCMC analysis with different values of σ_{r} until the best-fitting orbit resulted in a reduced χ^2 of unity for some optimal value of σ_{r}. We discuss the estimation of τ in the next subsection.

3.2 Estimation of τ

There is a degeneracy between σ_{r} and τ for the time sampling typical of our RV data: if we assume a long time-scale compared to the interval of time between the measurements, we are asserting that we have a reason to believe that several measurements may have been systematically offset in the same direction. A measurement that occurs within that time-scale but is offset to a very different extent from nearby measurements (e.g. if the correlation time-scale τ has been overestimated) will require a larger value of σ_{r} for the data set as a whole to yield a reduced χ^2 of unity.

To estimate τ, we looked at several data sets for each of the instruments HARPS, HIRES and SOPHIE. We repeated the analysis in Section 3.1 using values of τ in the range 0.1–5 d to check for weather-related correlations. To see the effects of choosing between an eccentric orbit and a circular orbit on our estimation of τ, we carried each the analysis twice by adjusting σ_{r} (see Section 3.1) to obtain a reduced χ^2 of unity (within 0.5 per cent) for each orbital model (circular and eccentric). We plotted the optimal values of σ_{r} against τ for several objects using data obtained from different instruments separately, as shown in Fig. 1. For WASP-2, we used our new HARPS measurements (Table 3) as well as SOPHIE measurements from Collier Cameron et al. (2007). For WASP-4 and WASP-5, we used our new HARPS measurements (Tables 4 and 5), and for HAT-P-7, we used our new SOPHIE measurements (Table 8) as well as HIRES measurements from Winn et al. (2009b). We found that for those data sets and objects where the orbital elements were well-constrained the plot showed a gentle increase in σ_{r} with τ, for $\tau \leq 1.5$ d, then increased much faster for these data sets at a time-scale of $\tau > 1.5$ d. For objects that have been observed with multiple instruments, this characteristic time-scale is independent both of the instrument used and of the assumption about the eccentricity (i.e. free eccentricity or e fixed at zero), suggesting that the correlated noise is probably related to weather conditions. We therefore assumed a correlation time-scale of 1.5 d in the rest of this study, unless otherwise noted. This means that we are accounting for the red noise in the same-night measurements, and for measurements that are taken further apart in time; this procedure reduces to the more familiar 'jitter' term. The value of σ_{r} inferred at $\tau = 1.5$ d in some cases varies by a few per cent depending on the model chosen, i.e. eccentric or circular, and varies across data sets, as discussed later.

We also investigated the effects of varying τ on our final results. For the same systems discussed above, we plotted the 95 per cent

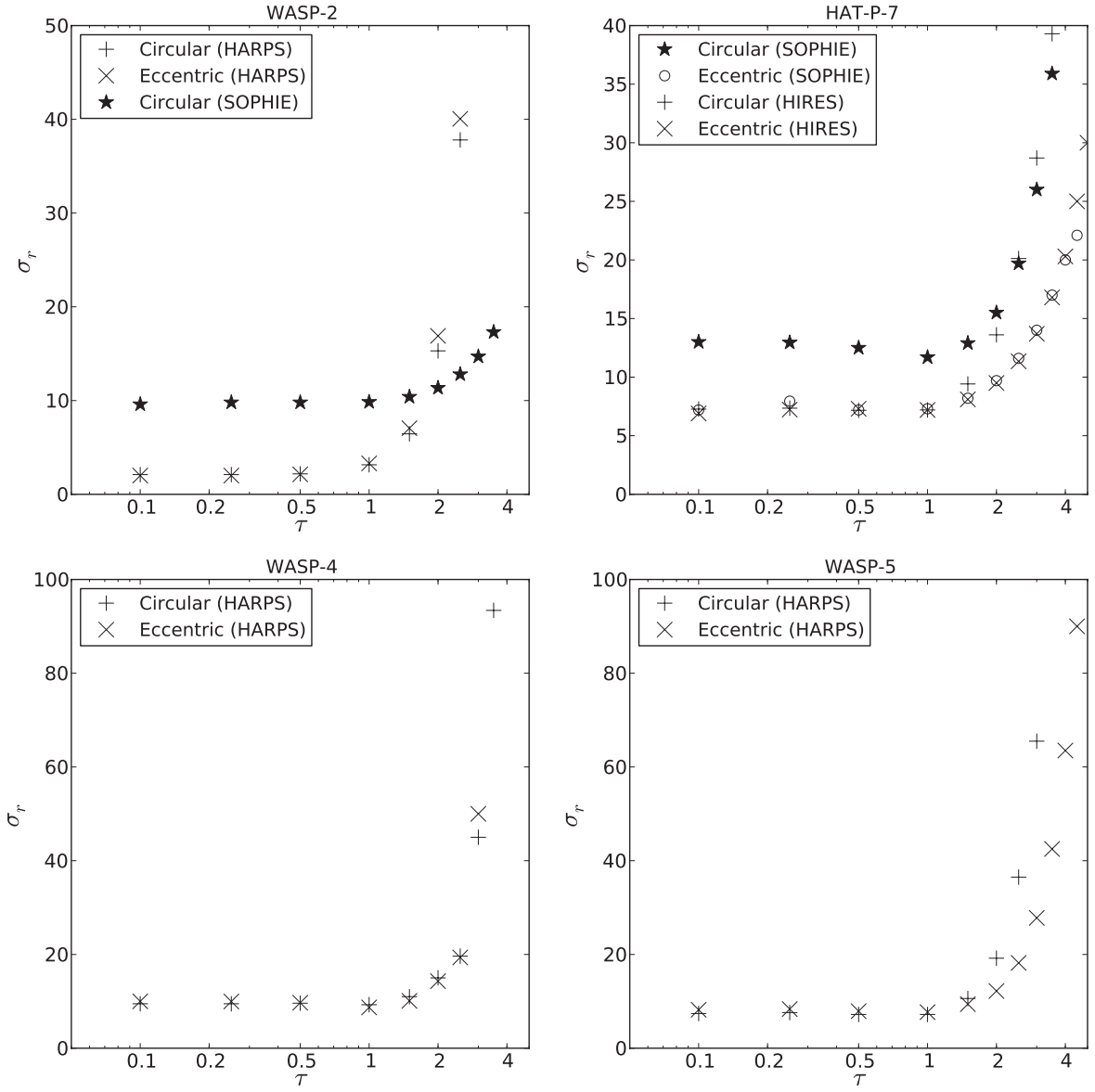

Figure 1. Plot showing the degeneracy between σ_r and τ for objects where the orbital parameters are well constrained (see Sections 3.1 and 3.2) because a sufficient number of RV measurements is available and provides sufficient phase coverage. The object being studied is shown in the title for each panel, and the instruments used for the measurements are shown in parenthesis. As can be seen on each plot, the optimal σ_r that gives a reduced χ^2 of unity for each data set increases slowly with τ for $\tau < 1.5$ d, but increases faster after 1.5 d. This hints that the systematic effects occur on a time-scale of 1.5 d, and could be related to the weather. Note the SOPHIE data for WASP-2 did not provide full phase coverage – the solution did not converge for an eccentric model and the knee at $\tau \sim 1.5$ d is less pronounced.

upper limit on the eccentricity as obtained from each data set separately. The results are shown in Fig. 2, where it is clear that the choice of τ has no effect on the final result for $\tau \geq 1.5$ d. The only exception is WASP-2 (HARPS), where we only have eight measurements and the phase coverage is not as complete as for the other objects (see Fig. 10). Similarly, the derived parameters V_0 and K did not vary appreciably with τ.

3.3 Model selection

Determining whether an orbit is consistent with circular (Model 1) or eccentric (Model 2) is an exercise in model selection. If we assume the prior probability of the circular and eccentric models is the same, we can use the BIC (Liddle 2007) to decide between the two models. This is equivalent to working out the Bayes factor $P(\text{data}|\text{Model}_1)/P(\text{data}|\text{Model}_2)$, subject to the assumptions described below. The Bayes factor is the ratio of marginal likelihoods for each model, each of which is given from

$$P(\text{data}|\text{Model}_\text{j}) = \int_{\Theta_j} L(\Theta_j|\text{data}) \times P(\Theta_j|\text{Model}_\text{j}) d\Theta_j, \qquad (7)$$

where Θ_j represent the vector of parameters for each model j, $L(\Theta_j|\text{data})$ is the likelihood and $P(\Theta_j|\text{Model}_\text{j})$ is the joint posterior distribution of the parameters.

As described in Section 3 and in Pont et al. (2009), the MCMC process produces the joint posterior distribution for the parameters, and we also obtain a maximum likelihood $L_{\max}$, corresponding to the smallest value of χ^2 (as given in Section 3.1) for each model.

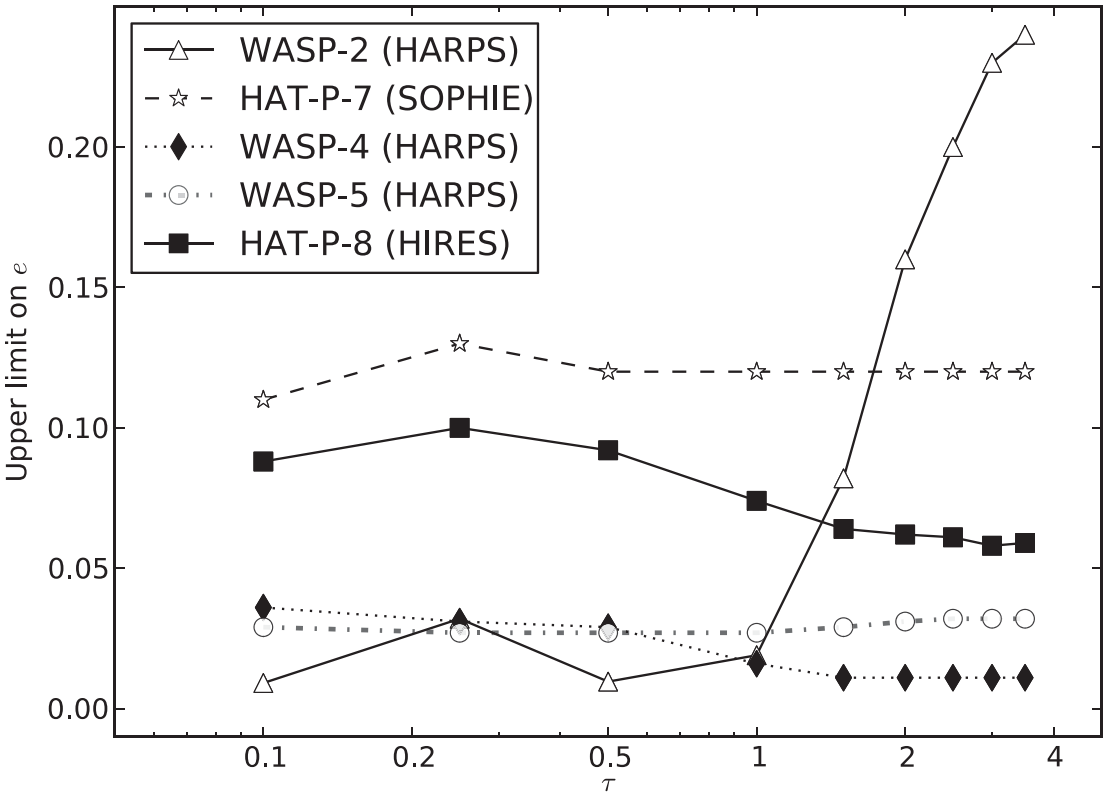

Figure 2. Plot showing the effect of varying τ on the 95 per cent upper limit on the derived eccentricity for WASP-2, HAT-P-7, WASP-4 and WASP-5. Except for WASP-2, where the phase coverage of the HARPS data is incomplete (see Fig. 10), varying τ has no effect on the 95 per cent upper limit of the derived eccentricity for time-scales of a few days, $\tau > 1.5$ d. Note: each line on this plot is made from a single data set.

We then use the BIC (Liddle 2007) as given by

$$\mathrm{BIC} = -2 \ln L_{\max} + k \ln N, \tag{8}$$

where N is the number of measurements and k is the number of parameters in the model used. This simplifies the expression for the marginal likelihood by performing the integration using Laplace's method and assumes a flat prior. If we replace $L_{\max}$ with the expression given by $\mathrm{P}(\boldsymbol{D}|\boldsymbol{\theta}, I)$ in equation (3),

$$\mathrm{BIC} = \chi^2_{\min} + k \ln N + \ln\left((2\pi)^N |\boldsymbol{C}|\right), \tag{9}$$

where $\chi^2_{\min}$ is the minimum value of χ^2 achieved by the model, N is the number of measurements, k is the number of parameters in the model and $|\boldsymbol{C}|$ is the determinant of the correlation matrix given in Section 3.1.

The RV data for a Keplerian orbit involve six free parameters: the period P, a reference time such as the mid-transit time $T_{\rm tr}$, a semi-amplitude K, a mean velocity offset V_0, the argument of periastron ω and the eccentricity e. Following Ford (2006), we use the two projected components $e\cos\omega$ and $e\sin\omega$ instead of e and ω to improve the efficiency of the MCMC exploration. In this study, we use the period P, mid-transit time $T_{\rm tr}$ and their corresponding uncertainties as a priori information. We thus count them as two additional measurements in the calculation of the BIC, while the number of free parameters in each model (circular or eccentric) is now decreased by two. In this case, a circular model would have two free parameters (V_0 and K), while an eccentric model would have four free parameters (V_0, K, e and ω).

The term $k\ln N$ thus penalizes a model with a larger number of parameters (e.g. an eccentric orbit), and we seek the model with smallest BIC. For each object, we repeated the MCMC analysis using the optimal value for $\sigma_{\rm r}$ for a circular orbit and an eccentric orbit separately, at $\tau = 1.5$ d, unless otherwise noted. We call these two families. For each family, we performed a fit with a circular model and an eccentric model. In most cases, the two families agreed on a circular model (indicated by 'C' in Table 19) or an eccentric model (indicated by 'E' if $e > 0.1$ in Table 19), indicating this with a smaller $\mathrm{BIC_c}$ or a smaller $\mathrm{BIC_e}$, respectively. If the two families favoured a circular (or eccentric) orbit, we give the parameters from the family using an optimal value of $\sigma_{\rm r}$ for the circular (or eccentric) orbit. In a number of such cases, however, the upper limits on the orbital eccentricity were larger than $e = 0.1$. We labelled these eccentricities as 'poorly constrained' (indicated by 'P' in Table 19). In a few cases, the small number of measurements or the quality of measurements (e.g. for faint targets or low mass planets) meant the two families disagreed: the family using the optimal value of $\sigma_{\rm r}$ for a circular orbit gave a smaller value of $\mathrm{BIC_c}$, favouring the circular orbit and the family using the optimal value of $\sigma_{\rm r}$ for an eccentric orbit gave a smaller value of $\mathrm{BIC_e}$, favouring the eccentric orbit. We labelled these cases as 'poorly constrained' as well.

4 RESULTS

The results of this study are shown in Table 19. We place constraints on the eccentricities of transiting planets for which enough data is available. We analysed RV data for 54 systems. For eight systems, we used our new RV data (described in Section 2) in addition to existing RVs from the literature. For the other 46 systems, we reanalysed existing RVs from the literature.

In Section 4.1, we describe the planets for which we do not consider the evidence for an orbital eccentricity compelling, despite

previous evidence of a departure from circularity ($e > 1\sigma$ from zero), followed by Section 4.2, where we describe the planets for which we consider the orbital eccentricity to be either so small as to be undetectable or compatible with zero. In Section 4.3 we describe planets that can be safely considered to be on eccentric orbits and, finally, in Section 4.4 we describe the planets for which we consider the orbital eccentricity to be poorly constrained (as described in Section 3.3). In the following sections we also include a discussion of the evidence for eccentricity for 26 other systems from the literature.

4.1 Planets with orbits that no longer qualify as eccentric according to this study

In a number of cases in the past, the derived eccentricity from an MCMC analysis deviated from zero by more than 1σ, for example CoRoT-5b, GJ436b, WASP-5b, WASP-6b, WASP-10b, WASP-12b, WASP-14b, WASP-17b and WASP-18b. In this section, we discuss the cases of seven planets, CoRoT-5b, WASP-6b, WASP-10b, WASP-12b, WASP-17b, WASP-18b and WASP-5b, that are shown to have orbital eccentricities that are compatible with zero.

CoRoT-5

CoRoT-5b is a 0.46 M_j planet on a 4.03 d orbit around an F9 star ($V = 14.0$), first reported by Rauer et al. (2009). Using six SOPHIE measurements (one of which is during the spectroscopic transit, which we ignore in this study) and 13 HARPS measurements, the authors derived a value of eccentricity $e = 0.09^{+0.09}_{-0.04}$. In our study, we used the formal uncertainties quoted with the data without any additional noise treatment, since they resulted in a reduced χ^2 less than unity for both an eccentric and a circular orbit. We imposed the prior information from photometry $P = 4.037\,8962(19)$ and $T_{\rm tr} = 2454\,400.19885(2)$ from the Rauer et al. (2009) and obtained a value of $\chi^2_{\rm c} = 15.97$ for the circular orbit and a value of $\chi^2_{\rm e} = 13.50$ for the eccentric orbit ($e = 0.086^{+0.086}_{-0.054}$, $e < 0.26$). Using $N = 20$, $k = 3$ and $k = 5$ for the circular (two data sets, each with one V_0 and a single K) and eccentric orbits, respectively, we obtained $\mathrm{BIC_c} = 151.05$ and $\mathrm{BIC_e} = 154.57$. A smaller value of $\mathrm{BIC_c}$ means the circular orbit cannot be excluded.

WASP-6

WASP-6b is a 0.50 M_j planet on a 3.36 d orbit around a G8 star (V = 11.9), first reported by Gillon et al. (2009b). Using 35 CORALIE measurements and 44 HARPS measurements (38 of which occur near or during a spectroscopic transit, which we ignore in this study), the authors derived a value of eccentricity $e = 0.054^{+0.018}_{-0.015}$. In our study, we used the 35 CORALIE measurements and the six HARPS measurements that were not taken in the single night where the spectroscopic transit was observed. We used $\sigma_{\rm r} = 0\,\mathrm{m\,s^{-1}}$ for CORALIE (the data produce a reduced $\chi^2 = 0.89$ when fitted with a circular orbit, indicating overfitting) but for HARPS we used $\tau = 1.5$ d and $\sigma_{\rm r} = 4.15\,\mathrm{m\,s^{-1}}$ to obtain a reduced χ^2 of unity for the circular orbit. We obtained a value of $\chi^2_{\rm c} = 38.09$ for the circular orbit and a value of $\chi^2_{\rm e} = 33.58$ for the eccentric orbit ($e = 0.041 \pm 0.019$, $e < 0.075$). Using $N = 43$ (41 RVs and two constraints from photometry), $k = 3$ and $k = 5$ for the circular (two data sets, each with one V_0 and a single K) and eccentric orbits, respectively, we obtained $\mathrm{BIC_c} = 333.25$ and $\mathrm{BIC_e} = 336.27$. We repeated the calculations, using $\sigma_{\rm r} = 0$ for CORALIE (the data produce a reduced $\chi^2 = 0.85$ when fitted with an eccentric orbit, indicating overfitting) but for HARPS we used $\tau = 1.5$ d and $\sigma_{\rm r} = 3.59\,\mathrm{m\,s^{-1}}$ to obtain a reduced χ^2 of unity for the eccentric orbit. We obtained a value of $\chi^2_{\rm c} = 39.20$ for the circular orbit and a value of $\chi^2_{\rm e} = 34.47$ for the eccentric orbit ($e = 0.043 \pm 0.019$, $e < 0.075$). Using $N = 43$, $k = 3$ and $k = 5$ for the circular and eccentric orbits, respectively, we obtained $\mathrm{BIC_c} = 333.60$ and $\mathrm{BIC_e} = 336.39$. We therefore find that the circular orbital solution cannot be excluded, but the possibility that $e > 0.1$ is rejected.

WASP-10

WASP-10b is a 2.96 M_j planet on a 3.09 d orbit around a K5 star ($V = 12.7$), first reported by Christian et al. (2009). Using seven SOPHIE measurements and seven FIES measurements, the authors derived a value of eccentricity $e = 0.059^{+0.014}_{-0.004}$. The FIES data yielded a reduced χ^2 less than unity with both eccentric and circular orbits, indicating overfitting, so we set $\sigma_{\rm r} = 0\,\mathrm{m\,s^{-1}}$.

For the SOPHIE data, we used $\tau = 1.5$ d, $\sigma_{\rm r} = 54.5\,\mathrm{m\,s^{-1}}$ to obtain a reduced χ^2 of unity for the circular orbit. We reanalysed all the RV measurements, and applied the prior from photometry $P = 3.092\,7636(200)$ and $T_{\rm tr} = 2454\,357.8581(4)$ from Christian et al. (2009). We obtained a value of $\chi^2_{\rm c} = 13.49$ for the circular orbit and a value of $\chi^2_{\rm e} = 7.47$ for the eccentric orbit ($e = 0.049 \pm 0.022$, less significant than the original claim). Using 14 measurements and two priors from photometry ($N = 16$), $k = 3$ and $k = 5$ for the circular (two data sets, each with one V_0 and a single K) and eccentric orbits, respectively, we obtained $\mathrm{BIC_c} = 151.50$ and $\mathrm{BIC_e} = 151.01$. This now appears to show only a marginal support for an eccentric orbit.

We plotted the SOPHIE RV data against time, as shown in Fig. 3 and overplotted a circular orbit as well as an eccentric orbit. Due to the long time between the first two measurements and the last five, we plot them in separate panels, shown on the left and right, respectively. It is clear that the first measurement is pulling the eccentricity upwards, and we suspect from experience that the long-term drifts in the SOPHIE zero-point in HE mode for faint targets could have affected the first two measurements. We therefore repeated our calculations using only the last five measurements from the SOPHIE data set and the whole FIES data set, and set $\sigma_{\rm r} = 45.5\,\mathrm{m\,s^{-1}}$ for SOPHIE. This time, we obtained a value of $\chi^2_{\rm c} = 11.81$ for the circular orbit and a value of $\chi^2_{\rm e} = 7.64$ for the eccentric orbit ($e = 0.043 \pm 0.035$). Using 12 measurements and two priors from photometry ($N = 14$), $k = 3$ and $k = 5$ for the circular (two data sets, each with one V_0 and a single K) and eccentric orbits, respectively, we obtained $\mathrm{BIC_c} = 128.71$ and $\mathrm{BIC_e} = 129.83$, this time favouring the circular orbit. We repeated this calculation, and set $\sigma_{\rm r} = 0\,\mathrm{m\,s^{-1}}$ for both SOPHIE and FIES, as each data set gave a reduced χ^2 of less than unity for the eccentric orbit (SOPHIE reduced $\chi^2 = 0.64$, FIES reduced $\chi^2 = 0.45$). This time, we obtained a value of $\chi^2_{\rm c} = 19.30$ for the circular orbit and a value of $\chi^2_{\rm e} = 10.65$ for the eccentric orbit ($e = 0.080 \pm 0.055$). Using 12 measurements and two priors from photometry ($N = 14$), $k = 3$ and $k = 5$ for the circular (two data sets, each with one V_0 and a single K) and eccentric orbits, respectively, we obtained $\mathrm{BIC_c} = 128.33$ and $\mathrm{BIC_e} = 124.97$, this time favouring the eccentric orbit once again. It is therefore unclear to us whether or not the orbital eccentricity is non-zero as claimed in Christian et al. (2009).

Maciejewski et al. (2011a) used transit timing variation analysis and reanalysed the RV data to obtain an eccentricity that is indistinguishable from zero ($e = 0.013 \pm 0.063$). They argued instead that the original detection of an eccentricity had been influenced by starspots. The difference between our value of eccentricity and that derived by Maciejewski et al. (2011a) is probably due to the fact that the latter used a two-planet model, which can reduce the derived eccentricity further – sparse sampling of the RV from a two-planet system can lead to an overestimated eccentricity.

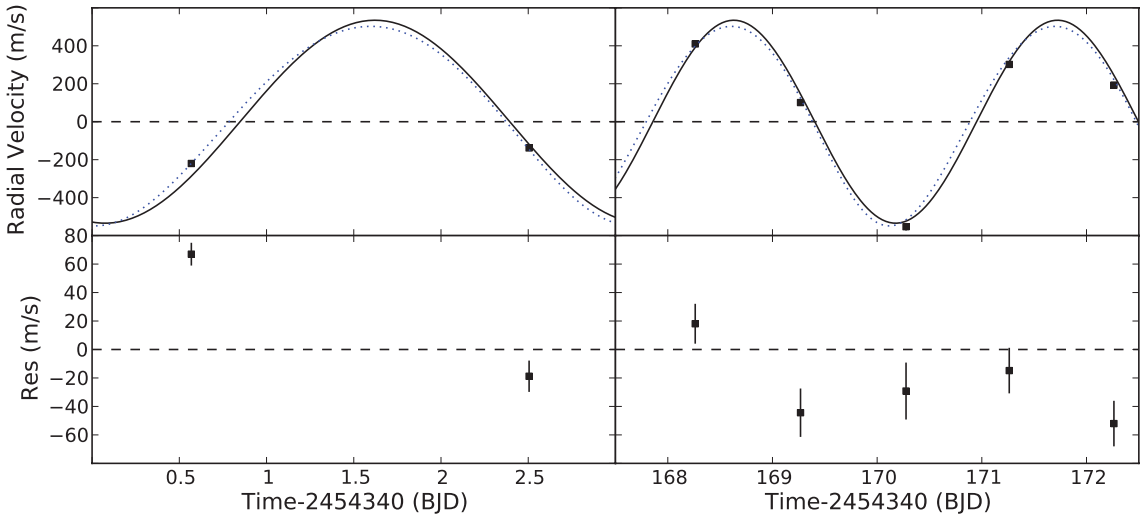

Figure 3. Plot showing SOPHIE RV data from Christian et al. (2009) for WASP-10, plotted against time. The plot has been split along the time axis into two panels (left and right) to remove the 160 d without measurements, for clarity. A circular orbit (solid line) and an orbit with the best-fitting eccentricity ($e = 0.048$) are overplotted. The residuals relative to the circular orbit are shown in the bottom panel.

WASP-12

WASP-12b is a 1.41 M_j planet on a 1.09 d orbit around an F9 star (V =11.7), first reported by Hebb et al. (2009). Using SOPHIE measurements, the original authors derived a value of eccentricity $e = 0.049 \pm 0.015$. Husnoo et al. (2011) used new SOPHIE RV measurements, as well as the original transit photometry from Hebb et al. (2009) and the secondary eclipse photometry from Campo et al. (2011) to suggest that the eccentricity was in fact compatible with zero ($e = 0.017^{+0.015}_{-0.010}$).

WASP-17

WASP-17b is a 0.50 M_j planet on a 3.74 d orbit around an F6 star (V = 11.6), first reported by Anderson et al. (2010). Using 41 CORALIE measurements (three of which are during the spectroscopic transit, which we ignore in this study) and three HARPS measurements, the authors considered three cases: first imposing a prior on the mass M_* of the host star, secondly imposing a main-sequence prior on the stellar parameters and thirdly with a circular orbit. They derived values of eccentricity $e = 0.129^{+0.106}_{-0.068}$ and $e = 0.237^{+0.068}_{-0.069}$ for the first two cases, respectively. We set $\sigma_r = 0$ for both HARPS and CORALIE since we obtained a reduced χ^2 of slightly less than unity for both eccentric and circular orbits for either data set alone, indicating overfitting. We obtained a value of $\chi^2_c = 37.98$ for the circular orbit and a value of $\chi^2_e = 35.94$ for the eccentric orbit. Using 41 measurements and two priors from photometry ($N = 43$), $k = 3$ and $k = 5$ for the circular (two data sets, each with one V_0 and a single K) and eccentric orbits, respectively, we obtained $\mathrm{BIC_c} = 399.31$ and $\mathrm{BIC_e} = 404.80$. We thus find that the circular orbit cannot be excluded, agreeing with the third case ($e = 0$, fixed) considered in Anderson et al. (2010) and rejecting the two derived values of eccentricity in that paper.

WASP-18

WASP-18b is a 10.3 M_j planet on a 0.94 d orbit around an F6 star ($V = 9.3$), first reported by Hellier et al. (2009a). Using nine CORALIE measurements (we drop the third measurement in our final analysis, since it produces a 5σ residual that is not improved by an eccentric orbit, suggesting that it is a genuine outlier), the authors derived a value of eccentricity $e = 0.0092 \pm 0.0028$. In our study, we set $\tau = 1.5$ d and $\sigma_r = 20.15\,\mathrm{m\,s^{-1}}$ to obtain a reduced χ^2 of unity for the circular orbit. We obtained a value of $\chi^2_c = 8.17$ for the circular orbit and a value of $\chi^2_e = 6.64$ for the eccentric orbit ($e = 0.007 \pm 0.005$, $e < 0.018$). Using $N = 10$, $k = 2$ and $k = 4$ for the circular (one data set, with one V_0 and a single K) and eccentric orbits, respectively, we obtained $\mathrm{BIC_c} = 75.34$ and $\mathrm{BIC_e} = 78.41$. We repeated the calculations using $\sigma_r = 22.5\,\mathrm{m\,s^{-1}}$ to obtain a reduced χ^2 of unity for the eccentric orbit. We obtained a value of $\chi^2_c = 7.14$ for the circular orbit and a value of $\chi^2_e = 6.00$ for the eccentric orbit ($e = 0.008 \pm 0.005$, $e < 0.019$). Using $N = 10$, $k = 2$ and $k = 4$ for the circular (one data set, with one V_0 and a single K) and eccentric orbits, respectively, we obtained $\mathrm{BIC_c} = 75.50$ and $\mathrm{BIC_e} = 78.97$. We thus find that the circular orbit cannot be excluded, in contrast to Hellier et al. (2009a). The possibility that $e > 0.1$ is excluded.

WASP-5 (new HARPS data)

WASP-5b is a 1.6 M_j planet on a 1.63 d orbit around a G4 star ($V = 12.3$), first reported by Anderson et al. (2008). Gillon et al. (2009a) used z-band transit photometry from the VLT to refine the eccentricity to $e = 0.038^{+0.026}_{-0.018}$, and the authors made a tentative claim for the detection of a small eccentricity. We analysed our 11 new HARPS measurements for WASP-5 and the 11 CORALIE RVs from Anderson et al. (2008) using the photometric constraints on the orbital period $P = 1.628\,4246(13)$ and mid-transit time $T_{tr} = 2454\,375.624\,956(24)$ from Southworth et al. (2009).

We use $\tau = 1.5$ d, $\sigma_r = 10.6\,\mathrm{m\,s^{-1}}$ for HARPS and $\sigma_r = 4.3\,\mathrm{m\,s^{-1}}$ for CORALIE to obtain a value of reduced χ^2 of unity for the circular orbit for each data set separately. We ran the MCMC twice: the first time fitting for the systemic velocity v_0 and semi-amplitude K, and the second time adding two parameters $e\cos\omega$ and $e\sin\omega$ to allow for an eccentric orbit. The best-fitting result is shown in Fig. 4. The residuals for a circular orbit are plotted, and a signal is clearly present in the residuals. The value of χ^2 for the circular orbit is 24.36 and that for an eccentric orbit is 20.57. This results in a value of $\mathrm{BIC_c} = 169.40$ for the circular orbit and $\mathrm{BIC_e} = 171.97$ for

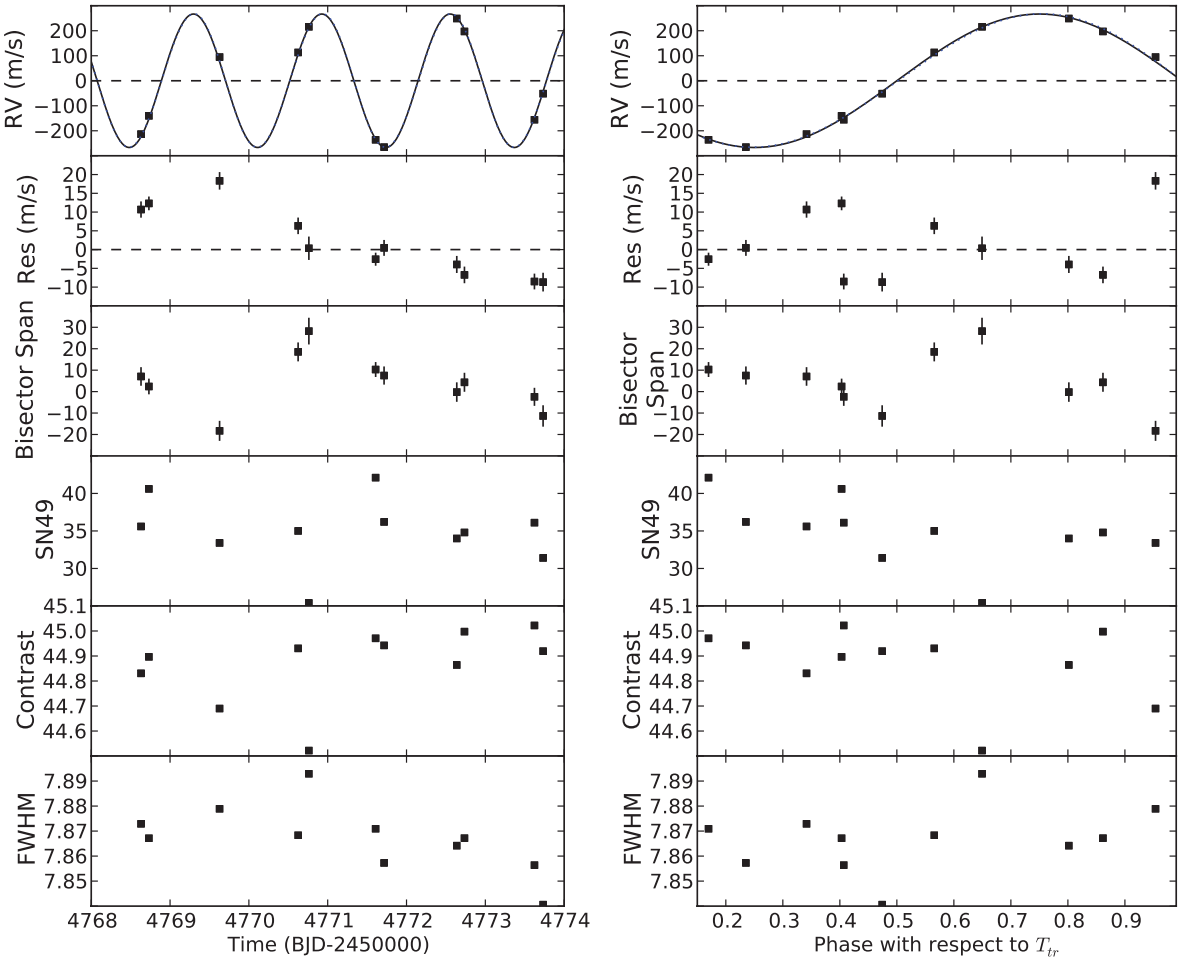

Figure 4. HARPS measurements of WASP-5 plotted against time (left) and phase with respect to the mid-transit time $T_{\rm tr}$ (right). In each case, a solid line is overplotted to represent a circular orbit and the residuals are plotted for this circular orbit. It is clear that a signal is present in the residuals (see text). An eccentric orbit with the best-fitting value of $e = 0.012$ is overplotted in both panels with a dotted line, but it is indistinguishable from the circular solution at this scale. Note the trend that is apparent in the residuals (second panel from the top on both the time and phase plots). We correct for this using a linear acceleration term in our model (see Fig. 5).

the eccentric orbit, given 22 measurements, two constraints from photometry and three and five free parameters, respectively, for each model.

We repeated the above analysis using $\tau = 1.5$ d, $\sigma_{\rm r} = 9.4\,{\rm m\,s^{-1}}$ for the HARPS data set to obtain a value of reduced χ^2 of unity for the eccentric orbit and $\sigma_{\rm r} = 0\,{\rm m\,s^{-1}}$ for CORALIE (which resulted in a reduced χ^2 of 0.58). This time, we obtained a value of χ^2 for the circular orbit, 27.35, and that for an eccentric orbit, 23.00. This leads to a value of $\rm BIC_c = 170.37$ for the circular orbit and $\rm BIC_e = 172.38$ for the eccentric orbit. Once again, the circular orbit is favoured.

A Keplerian model, circular or eccentric ($e = 0.012 \pm 0.007$), does not account for the scatter in the data the HARPS data set as shown in Fig. 4. We have therefore plotted the RV measurements, the bisector span, the signal-to-noise ratio at order 49, the contrast and full width at half-maximum for the cross-correlation function against the same time axis. The trend in RV residuals can be seen to be correlated with both the bisector span and the full width at half-maximum of the cross-correlation function. This suggests a line shape change that is related to either weather effects or instrumental systematics. The time-scale of this variation is compatible with both scenarios. The bisector inverse span is generally directly correlated with the residuals, which weighs against a scenario involving stellar activity, but this is not so clear for the first three measurements – the drift could be due to stellar activity or an additional planetary or stellar companion.

We extended the model with a linear acceleration of the form

$$v(t) = v_{\rm keplerian}(t) + \dot{\gamma}(t - t_0), \tag{10}$$

and fitted the HARPS data alone using $t_0 = 245\,4768$ (to allow the MCMC to explore values of $\dot{\gamma}$ more efficiently) and reran the MCMC twice: once for a circular orbit and once for an eccentric orbit. First, we used $\sigma_{\rm r} = 10.6\,{\rm m\,s^{-1}}$ for the HARPS data set, and the linear trend for a circular orbit resulted in $\dot{\gamma} = -2.6 \pm 2.9\,{\rm m\,s^{-1}\,yr^{-1}}$ and that for an eccentric orbit is $\dot{\gamma} = -2.0 \pm 2.9\,{\rm m\,s^{-1}\,yr^{-1}}$. The best-fitting result is shown in Fig. 5 and the residuals for a circular orbit are plotted in the bottom panel. The value of χ^2 for the circular orbit is 10.24 and that for an eccentric orbit is 7.70. This results in a value of $\rm BIC_{c,lin} = 71.91$ for the circular orbit and $\rm BIC_{e,lin} = 74.49$ for the eccentric orbit, given 11 (N = 13) measurements, two constraints from photometry and three and five free parameters, respectively, for each model. We repeated these calculations using $\sigma_{\rm r} = 9.4\,{\rm m\,s^{-1}}$ for the HARPS data set, and the linear trend for a circular orbit resulted in $\dot{\gamma} = -3.7 \pm 1.3\,{\rm m\,s^{-1}\,yr^{-1}}$ and that

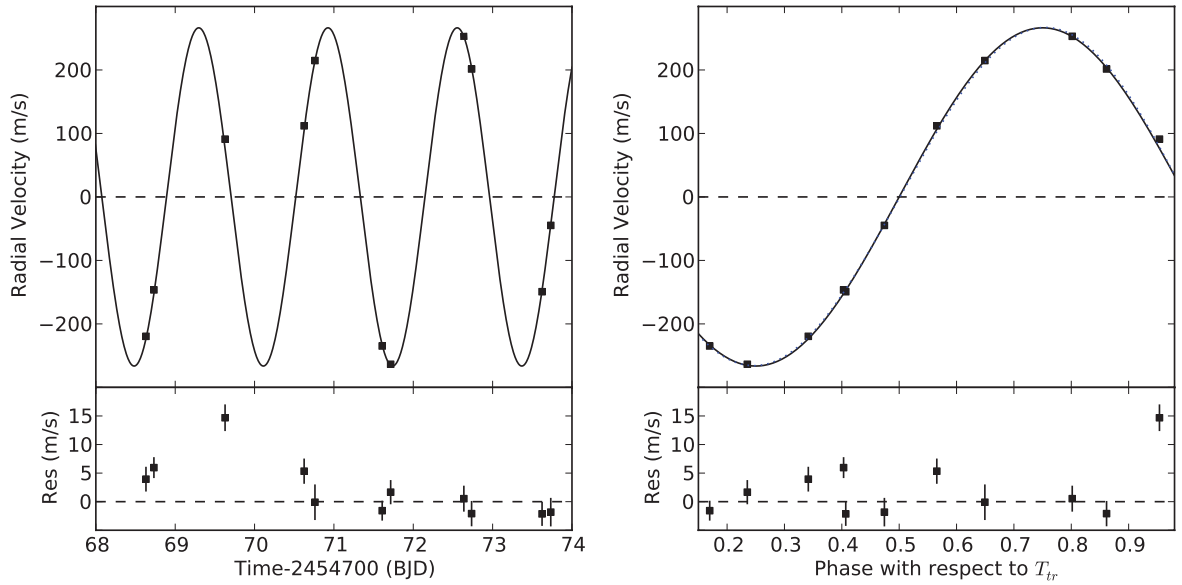

Figure 5. HARPS measurements of WASP-5 plotted against time (left) and phase with respect to the mid-transit time $T_{\rm tr}$ (right). In each case, a solid line is overplotted to represent a circular orbit and the residuals are plotted for this circular orbit. It is clear that a signal is present in the residuals (see text). A model for an eccentric orbit with the best-fitting value of $e = 0.013$ is overplotted in both panels with a dotted line, but it is indistinguishable from the circular solution at this scale. Both include the linear trend (see Section 4.2 and Fig. 4).

Table 11. System parameters for WASP-5. Left: Anderson et al. (2008). Right: results from our HARPS RV data alone, and results from using both our HARPS data and the original CORALIE data in Anderson et al. (2008). Median values for V_0 and K are quoted for the circular orbits, as well as 68.3 per cent confidence limits obtained from the eccentric solution (see section 'Analysis').

Parameter	Anderson et al. (2008)	HARPS only, This Work (with linear trend)	HARPS & CORALIE, This Work (no linear trend)
Centre-of-mass velocity V_0 [m s^{-1}]	20010.5 ± 3.4	20018 ± 12	20009.9 ± 7.4 (HARPS)
Orbital eccentricity e	0 (adopted)	0.013 ± 0.008 (<0.029)	0.012 ± 0.007 (<0.026)
Argument of periastron ω [^{o}]	0 (unconstrained)	0 (unconstrained)	0 (unconstrained)
$e \cos \omega$	–	0.002 ± 0.003	0.003 ± 0.003
$e \sin \omega$	–	0.012 ± 0.010	0.011 ± 0.009
Velocity semi-amplitude K [m s^{-1}]	277.8 ± 7.8	266.4 ± 1.3	266.9 ± 1.3

for an eccentric orbit is $\dot{\gamma} = -3.3 \pm 1.3\,{\rm m\,s^{-1}\,yr^{-1}}$. The value of χ^2 for the circular orbit is 15.46 and that for an eccentric orbit is 13.50. This leads to a value of $\mathrm{BIC_{c,lin}} = 69.72$ for the circular orbit and $\mathrm{BIC_{e,lin}} = 72.89$ for the eccentric orbit. The circular orbit is not excluded, and the possibility that $e > 0.1$ is excluded. The results for both models, one including the linear trend but excluding the CORALIE data, and one including the CORALIE data but excluding the linear trend, are shown in Table 11. In both cases, we give results for the case where $\sigma_{\rm r}$ is chosen to yield a reduced χ^2 of unity for the circular orbit. We attempted to repeat this using both the CORALIE and HARPS data sets, but we were unable to obtain a fit with the MCMC, because of the long time-scale between the two data sets.

4.2 Planets on circular orbits

We establish that 20 planets have orbital eccentricities compatible with zero and the 95 per cent upper limits are smaller than $e_{95} = 0.1$. In this section, we describe the planets WASP-4b, HAT-P-7b, TrES-2 and WASP-2b, for which we introduce new RVs. We also establish the 95 per cent upper limits on the eccentricities of WASP-5b, WASP-12b and WASP-18b, which have been described in Section 4.1. In addition, we give the 95 per cent upper limits on the eccentricities of CoRoT-1b, CoRoT-3b, HAT-P-8b, WASP-3b, WASP-16b, WASP-19b, WASP-22b, WASP-26b and XO-5b in Table 19. We discuss the evidence for circular orbits for HAT-P-13b, HD 189733b, HD 209458b and Kepler-5b at the end of this section.

WASP-4 (new HARPS data)

WASP-4b is a 1.2 M_j planet on a 1.34 d orbit around a G7 star (V = 12.5), first reported by Wilson et al. (2008). We analysed our 14 new HARPS measurements and the 14 CORALIE measurements from Wilson et al. (2008) for WASP-4 and used the photometric constraints on the orbital period $P = 1.338\,232\,14(71)$ and mid-transit time $T_{\rm tr} = 2454\,697.797\,562(43)$ from Winn et al. (2009a).

We estimate $\tau = 1.5$ d, $\sigma_{\rm r} = 11\,{\rm m\,s^{-1}}$ for the HARPS data set and $\sigma_{\rm r} = 4.5\,{\rm m\,s^{-1}}$ for the CORALIE data set to obtain a reduced χ^2 of unity for a circular orbit for each data set separately. We ran the MCMC twice: the first time fitting for the systemic velocity v_0 and semi-amplitude K only, i.e. a circular orbit ($k = 2$), and the

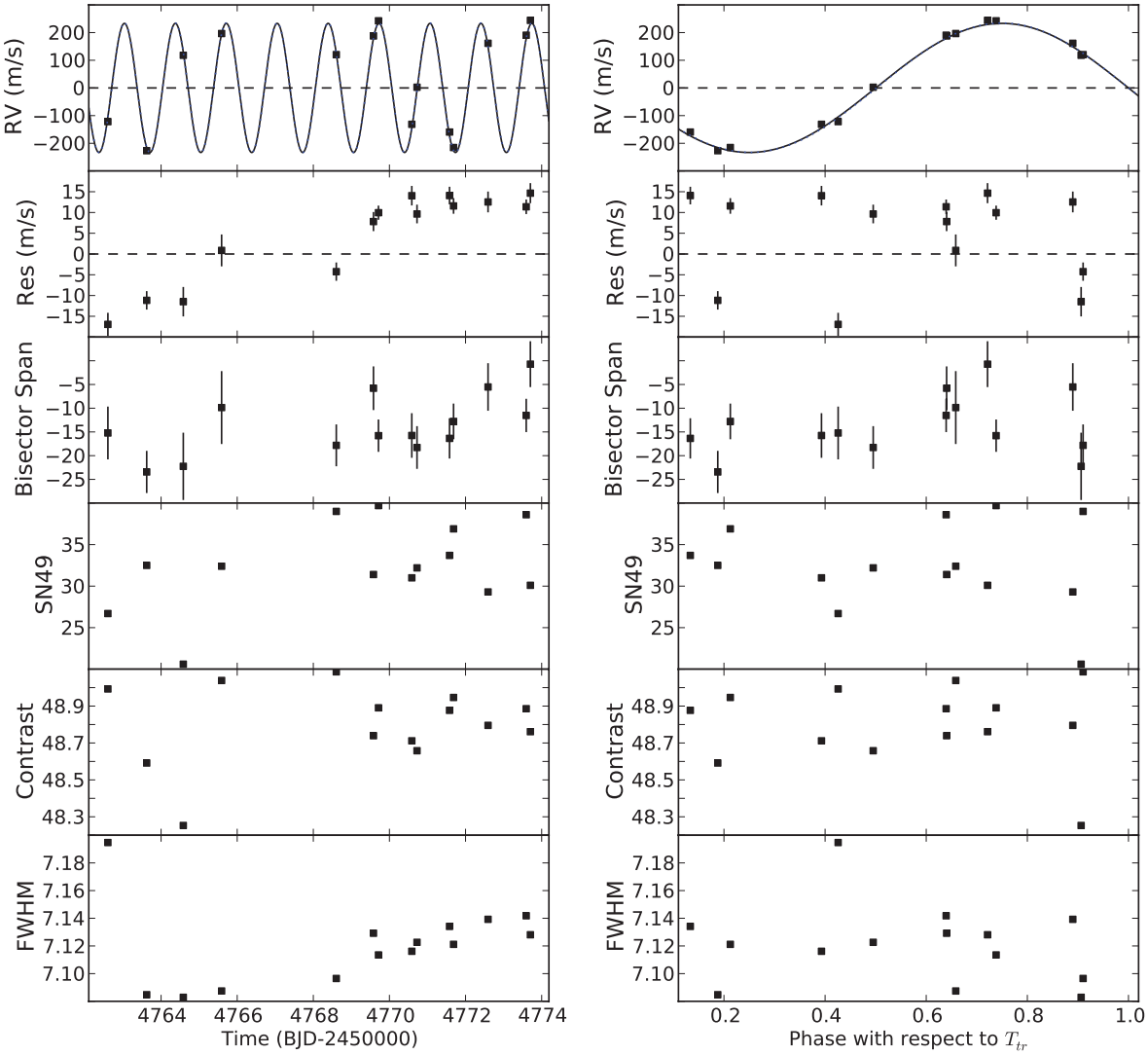

Figure 6. HARPS measurements of WASP-4 plotted against time (left) and phase with respect to the mid-transit time $T_{\rm tr}$ (right). In each case, a solid line is overplotted to represent a circular orbit and the residuals are plotted for this circular orbit. It is clear that a signal is present in the residuals (see text). An eccentric orbit with the best-fitting value of $e = 0.005$ is overplotted in both panels with a dotted line, but it is indistinguishable from the circular solution at this scale. Note the trend that is apparent in the residuals (second panel from the top on both images). We attempt to correct for this by repeating our calculations with a linear acceleration term in the model (see Section 4.2 and Fig. 7).

second time adding two parameters $e\cos\omega$ and $e\sin\omega$ to allow for an eccentric orbit ($k = 4$). The best-fitting result is shown in Fig. 6. The residuals for a circular orbit are plotted, and a signal is clearly present in the residuals. The value of χ^2 for the circular orbit is 27.13 and that for an eccentric orbit is 24.32. This leads to a value of $\mathrm{BIC_c} = 208.62$ for the circular orbit and $\mathrm{BIC_e} = 212.55$ for the eccentric orbit, given 14 measurements, two constraints from photometry and two and four free parameters, respectively, for each model.

We repeated the calculations, estimating $\tau = 1.5\,\mathrm{d}$, $\sigma_{\rm r} = 10.1\,\mathrm{m\,s^{-1}}$ for the HARPS data set and $\sigma_{\rm r} = 7.1\,\mathrm{m\,s^{-1}}$ for the CORALIE data set, to obtain a reduced χ^2 of unity for an eccentric orbit for each data set separately. The value of χ^2 for the circular orbit is 27.29 and that for an eccentric orbit is 24.33. This leads to a value of $\mathrm{BIC_c} = 208.72$ for the circular orbit and $\mathrm{BIC_e} = 212.51$.

Note the trend that is apparent in the residuals in Fig. 6. We have therefore plotted the RV measurements, the bisector span, the signal-to-noise ratio at order 49, the contrast and full width at half-maximum for the cross-correlation function against the same time axis. For most measurements, the trend in RV residuals can be seen to be correlated with both the bisector span and the full width at half-maximum of the cross-correlation function. This suggests a line shape change that is related to either stellar activity, weather effects or instrumental systematics. The time-scale of this variation is compatible with all three scenarios.

We repeated the calculations for the HARPS data set alone, and added a linear component to the RV model in the same way we did for WASP-5 in Section 4.1 and we set $t_0 = 2454\,762$ (to allow the MCMC to explore values of $\dot{\gamma}$ more efficiently) and reran the MCMC twice: once for a circular orbit and once for an eccentric orbit. We set $\tau = 1.5\,\mathrm{d}$ and $\sigma_{\rm r} = 11\,\mathrm{m\,s^{-1}}$ for the HARPS data set.

The best-fitting result is shown in Fig. 7. The residuals for a circular orbit are plotted, and a signal is clearly present in the residuals. The linear trend for a circular orbit results in $\dot{\gamma} = 1023 \pm 490\,\mathrm{m\,s^{-1}\,yr^{-1}}$ and that for an eccentric orbit is $\dot{\gamma} = 919 \pm 500\,\mathrm{m\,s^{-1}\,yr^{-1}}$.

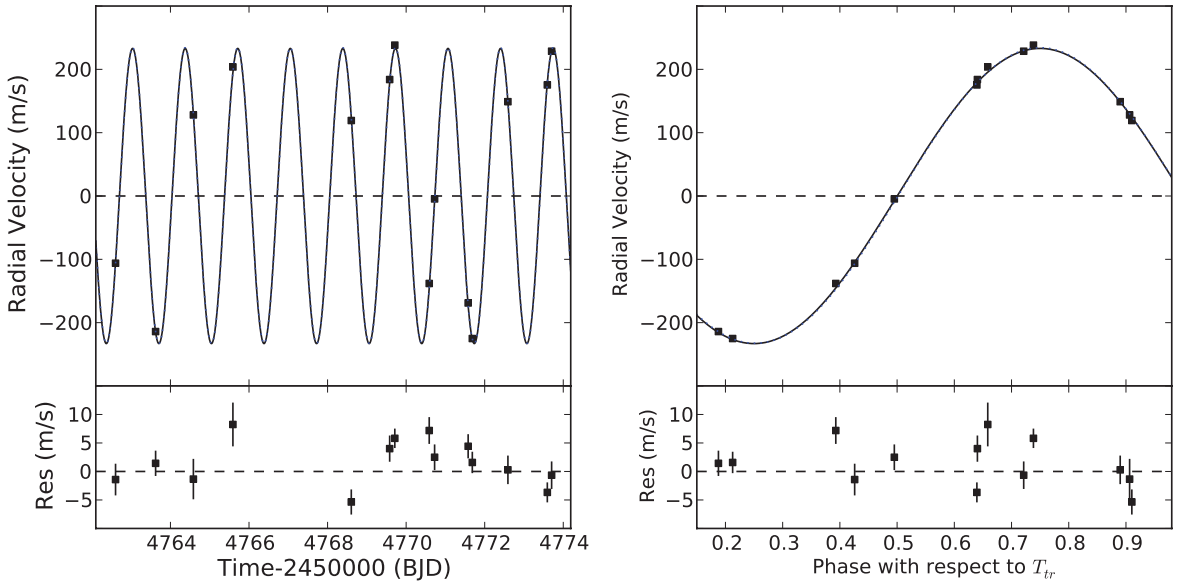

Figure 7. HARPS measurements of WASP-4 plotted against time (left) and phase with respect to the mid-transit time $T_{\rm tr}$ (right). In each case, a solid line is overplotted to represent a circular orbit and the residuals are plotted for this circular orbit. It is clear that a signal is present in the residuals (see text). An eccentric orbit with the best-fitting value of $e = 0.004$ is overplotted in both panels with a dotted line, but it is indistinguishable from the circular solution at this scale. The linear trend from Fig. 6 has now been included in the model.

Table 12. System parameters for WASP-4. Left: Wilson et al. (2008). Right: results from our HARPS RV data alone, and results from using both our HARPS data and the original CORALIE data in Wilson et al. (2008). Median values for V_0 and K are quoted for the circular orbits, as well as 68.3 per cent confidence limits obtained from the eccentric solution (see section 'Analysis').

Parameter	Wilson et al. (2008)	HARPS only, This Work (with linear trend)	HARPS and CORALIE, This Work (no linear trend)
Centre-of-mass velocity V_0 [m s^{-1}]	57733 ± 2	57773 ± 10	57790.8 ± 5.7
Orbital eccentricity e	0 (adopted)	0.004 ± 0.003 (<0.011)	0.005 ± 0.003 (<0.011)
Argument of periastron ω [^{o}]	0 (unconstrained)	0 (unconstrained)	0 (unconstrained)
$e \cos \omega$	–	0.004 ± 0.003	0.003 ± 0.003
$e \sin \omega$	–	−0.002 ± 0.004	−0.004 ± 0.004
Velocity semi-amplitude K [m s^{-1}]	240 ± 10	233.1 ± 2.1	233.7 ± 2.0

The value of χ^2 for the circular orbit is 9.83 and that for an eccentric orbit is 7.51. This leads to a value of $\mathrm{BIC_c} = 92.02$ for the circular orbit and $\mathrm{BIC_e} = 95.26$ for the eccentric orbit, given 14 measurements, two constraints from photometry and three and five free parameters, respectively, for each model.

We repeated the calculations, setting $\tau = 1.5$ d, $\sigma_{\rm r} = 10.05$ m s^{-1} for the HARPS data set. The value of χ^2 for the circular orbit is 10.30 and that for an eccentric orbit is 8.07. This leads to a value of $\mathrm{BIC_c} = 91.18$ for the circular orbit and $\mathrm{BIC_e} = 94.49$. In all cases, the circular orbit is not excluded. The results for both models, one including the linear trend but excluding the CORALIE data, and one including the CORALIE data but excluding the linear trend, are shown in Table 12. In both cases, we give results for the case where $\sigma_{\rm r}$ is chosen to yield a reduced χ^2 of unity for the circular orbit. We reject the possibility that $e > 0.1$.

HAT-P-7 (new SOPHIE data)

HAT-P-7b is a 1.8 M_j planet on a 2.20 d orbit around an F6 star (V = 10.5), first reported by Pál et al. (2008). We use 13 new SOPHIE RV measurements and 16 out of the 17 HIRES measurements in Winn et al. (2009b) (we drop one in-transit measurement) to work out the orbital parameters of HAT-P-7b. We impose the period $P = 2.204\,733(10)$ d as given from photometry in Welsh et al. (2010) and mid-transit time $T_{\rm tr} = 245\,4731.679\,29(43)$ BJD as given from photometry in Winn et al. (2009b). We set $\tau = 1.5$ d, $\sigma_{\rm r} = 9.41$ m s^{-1} for HIRES and $\sigma_{\rm r} = 12.9$ m s^{-1} for SOPHIE to obtain a reduced χ^2 of unity for the best-fitting circular orbit for each data set separately. We used 29 measurements in all, and count the two constraints from photometry as two additional data points to obtain $N = 31$, and used $k = 4$ for the circular orbit [two V_0, one for each data set, the semi-amplitude K and a constant drift term $\dot{\gamma}$, since Winn et al. (2009b) found evidence for a distant companion in the system and we set $t_0 = 245\,4342$]. We repeated this analysis with an eccentric orbit $k = 6$ (4 degrees of freedom for the circular orbit with two data sets and a linear acceleration, and 2 additional degrees of freedom for the eccentricity, $e \cos \omega$ and $e \sin \omega$). The orbital parameters are given in Table 13, and the RV data set is plotted in Fig. 8, with residuals shown for a circular orbit. The figure also shows models of a circular and an eccentric orbit (with $e = 0.014$), but they are almost undistinguishable. For the circular orbit, we obtained

Table 13. System parameters for HAT-P-7. Left: Winn et al. (2009b). Right: results from our SOPHIE RV data. Median values for V_0 and K are quoted for the circular orbits, as well as 68.3 per cent confidence limits obtained from the eccentric solution. The upper 95 per cent limit is also given for the eccentricity from our analysis.

Parameter	HIRES, Winn et al. (2009b)	HIRES+SOPHIE, This Work
Centre-of-mass velocity V_0 [m s^{-1}]	-51.2 ± 3.6	-49.96 ± 6.0 (HIRES) and -10510 ± 10 (SOPHIE)
Orbital eccentricity e	$e_{99\,\mathrm{per\,cent}} < 0.039$	0.014 ± 0.010 ($e < 0.038$)
Argument of periastron ω [^{o}]	–	0 (unconstrained)
$e \cos\omega$	-0.0019 ± 0.0077	-0.007 ± 0.004
$e \sin\omega$	0.0037 ± 0.0124	-0.011 ± 0.015
Velocity semi-amplitude K [m s^{-1}]	211.8 ± 2.6	213.8 ± 1.2
Constant radial acceleration $\dot{\gamma}$ [m s^{-1} yr^{-1}]	21.5 ± 2.6	21.1 ± 4.2

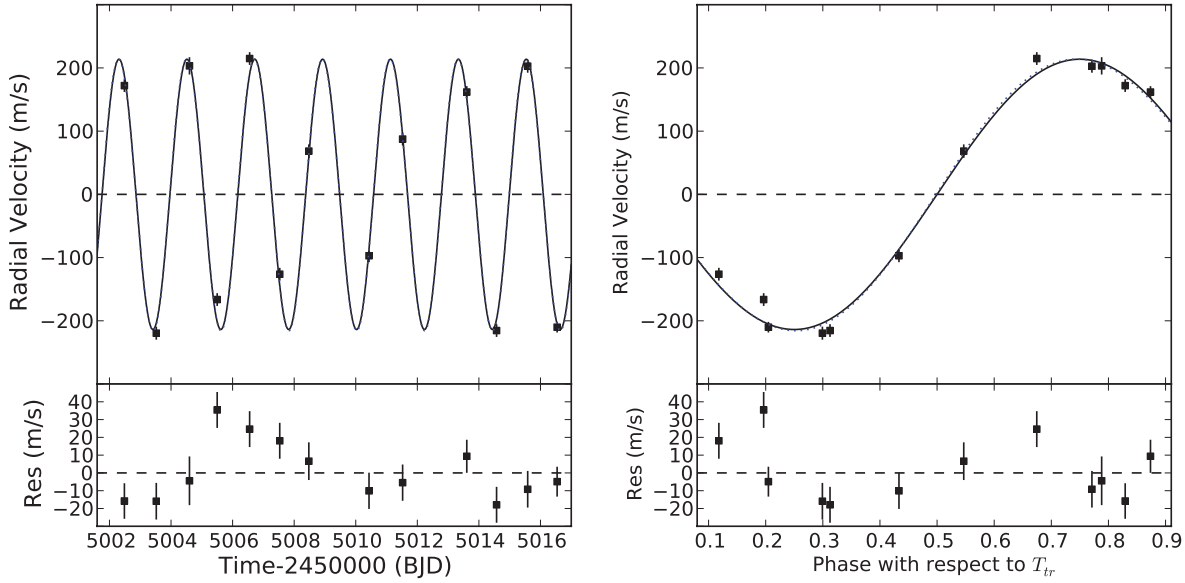

Figure 8. Plot showing our new SOPHIE RV data for HAT-P-7, plotted against time (left), and orbital phase (right) with respect to $T_{\rm tr}$. A circular orbit (solid line) and an orbit with the best-fitting eccentricity (dotted line, but almost undistinguishable from the circular solution since $e = 0.014$) are overplotted. The residuals relative to the circular orbit are shown in the bottom panels.

$\chi^2 = 26.94$, and a value of $\mathrm{BIC_c} = 222.81$ and for the eccentric orbit, we obtained $\chi^2 = 23.98$ and a value of $\mathrm{BIC_e} = 226.72$. We repeated the calculations and set $\tau = 1.5$ d, $\sigma_{\rm r} = 8.2\,\mathrm{m\,s^{-1}}$ for HIRES and $\sigma_{\rm r} = 8.2\,\mathrm{m\,s^{-1}}$ for SOPHIE to obtain a reduced χ^2 of unity for the best-fitting eccentric orbit. For the circular orbit, we obtained $\chi^2 = 35.65$ and a value of $\mathrm{BIC_c} = 224.14$; and for the eccentric orbit, we obtained $\chi^2 = 31.89$ and a value of $\mathrm{BIC_e} = 227.25$. We therefore find that the circular orbit cannot be excluded for HAT-P-7b. Further, we exclude the possibility that $e > 0.1$.

TrES-2 (new SOPHIE data)

TrES-2b is a 1.3 M_j planet on a 2.47 d orbit around a G0 star ($V = 11.4$), first reported by O'Donovan et al. (2006). We use 10 new SOPHIE RV measurements and the 11 HIRES measurements in O'Donovan et al. (2006) to work out the orbital parameters of TrES-2b. We impose the period $P = 2.470\,614(1)$ d and mid-transit time $T_{\rm tr} = 2453\,957.634\,92(13)$ BJD as given from photometry in Raetz et al. (2009).

We set $\tau = 1.5$ d and $\sigma_{\rm r} = 6.8\,\mathrm{m\,s^{-1}}$ for SOPHIE to obtain a reduced χ^2 of unity for the best-fitting circular orbit (using the SOPHIE data alone), and set $\sigma_{\rm r} = 0\,\mathrm{m\,s^{-1}}$ for the HIRES data since a circular orbit for that data set alone yields a reduced χ^2 of 0.72, indicating over-fitting. We used 21 measurements in all, and count the two constraints from photometry as two additional data points to obtain $N = 23$, and used $k = 3$ for the circular orbit (two V_0, one for each data set, and the semi-amplitude K). We repeated this analysis with an eccentric orbit $k = 5$ (3 degrees of freedom for the circular orbit, and 2 additional degrees of freedom for the eccentricity, $e \cos\omega$ and $e \sin\omega$). The orbital parameters are given in Table 14, and the RV data set is plotted in Fig. 9, with residuals shown for a circular orbit. The figure also shows models of a circular and an eccentric orbit (with $e = 0.023$), but they are almost undistinguishable. For the circular orbit, we obtained $\chi^2 = 18.00$, yielding a value of $\mathrm{BIC_c} = 160.30$ and for the eccentric orbit, we obtained $\chi^2 = 15.91$ and a value of $\mathrm{BIC_e} = 164.48$. We repeated the calculations and set $\sigma_{\rm r} = 8.45\,\mathrm{m\,s^{-1}}$ for SOPHIE to obtain a reduced χ^2 of unity for the best-fitting circular orbit (using the SOPHIE data alone), while we set $\sigma_{\rm r} = 0\mathrm{m\,s^{-1}}$ for the HIRES data since an eccentric orbit for that data set alone yields a reduced χ^2 of 0.56, indicating over-fitting. For a circular orbit, we obtained $\chi^2 = 15.97$, resulting in a value of $\mathrm{BIC_c} = 159.38$ and for an eccentric orbit, we obtained $\chi^2 = 13.88$ and a value of $\mathrm{BIC_e} = 163.56$. We therefore find that the circular orbit cannot be excluded for TrES-2b. Furthermore, we exclude the possibility that $e > 0.1$.

WASP-2 (new HARPS data)

WASP-2b is a 0.85 M_j planet on a 2.15 d orbit around a K1 star ($V = 12$), first reported by Collier Cameron et al. (2007). We

Table 14. System parameters for TrES-2. Left: O'Donovan et al. (2006). Right: results from our HARPS RV data. Median values for V_0 and K are quoted for the circular orbits, as well as 68.3 per cent confidence limits obtained from the eccentric solution. The 95 per cent limit on the eccentricity is also given.

Parameter	HIRES, O'Donovan et al. (2006)	HIRES, SOPHIE, This Work
Centre-of-mass velocity V_0 [m s^{-1}]	–	-29.8 ± 2.4 (HIRES), -315.5 ± 5.0 (SOPHIE)
Orbital eccentricity e	0 (adopted)	0.023 ± 0.014, $e < 0.051$
Argument of periastron ω [^{o}]	0 (unconstrained)	0 (unconstrained)
$e \cos \omega$	–	0.002 ± 0.009
$e \sin \omega$	–	-0.022 ± 0.016
Velocity semi-amplitude K [m s^{-1}]	181.3 ± 2.6	181.1 ± 2.5

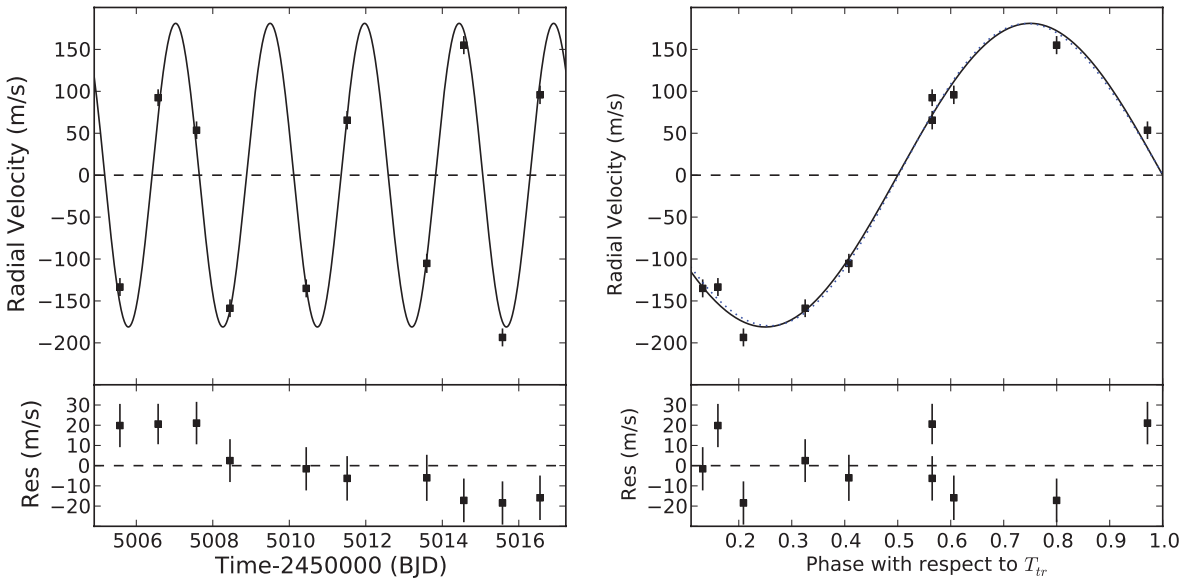

Figure 9. Plot showing our new SOPHIE RV data for TrES-2, plotted against time (left) and orbital phase with respect to $T_{\rm tr}$ (right). A circular orbit (solid line) and an orbit with the best-fitting eccentricity (dotted line, but almost undistinguishable from the circular solution since $e = 0.023$) are overplotted. The residuals relative to the circular orbit are shown in the bottom panel.

use eight new HARPS RV measurements and seven of the original nine SOPHIE measurements (we drop the first measurement, which has an uncertainty of about 15 times larger than the rest, and the fifth, which shows a 3σ deviation at a phase close to the transit) in Collier Cameron et al. (2007) to work out the orbital parameters of WASP-2b. We impose the period $P = 2.152\,221\,44(39)$ d and mid-transit time $T_{\rm tr} = 2453\,991.514\,55(17)$ BJD as given from photometry in Southworth et al. (2010). We used 15 measurements in all, and count the two constraints from photometry as two additional data points ($N = 17$) and used $k = 3$ for the circular orbit (two V_0, one for each data set, and the semi-amplitude K).

We estimated the time-scale of correlated noise for both the HARPS and SOPHIE data to be $\tau = 1.5$ d, and we estimated $\sigma_{\rm r} = 10.4$ m s^{-1} for the SOPHIE data and $\sigma_{\rm r} = 6.45$ m s^{-1} for the HARPS data to obtain a reduced χ^2 of unity for the circular orbit. We repeated this analysis with an eccentric orbit $k = 5$ (3 degrees of freedom for the circular orbit, and 2 additional degrees of freedom for the eccentricity, $e \cos \omega$ and $e \sin \omega$). The orbital parameters are given in Table 15, and the RV data set is plotted in Fig. 10, with residuals shown for a circular orbit. The figure also shows models of a circular and an eccentric orbit (with $e = 0.027$), but they are almost undistinguishable. For the circular orbit, we obtained $\chi^2 = 15.60$, giving a value of $\mathrm{BIC_c} = 115.08$ and for the eccentric

Table 15. System parameters for WASP-2. Left: Collier Cameron et al. (2007). Right: results from our HARPS RV data. Median values for V_0 and K are quoted for the circular orbits, as well as 68.3 per cent confidence limits obtained from the eccentric solution (see section Analysis) and 95 per cent limit on eccentricity.

Parameter	SOPHIE, Collier Cameron et al. (2007)	SOPHIE and HARPS, This Work
Centre-of-mass velocity V_0 [m s^{-1}]	-27863 ± 7	-27862 ± 7.4 (SOPHIE), -27739.81 ± 4.1 (HARPS),
Orbital eccentricity e	0 (adopted)	0.027 ± 0.023 (<0.072)
Argument of periastron ω [^{o}]	0 (unconstrained)	0 (unconstrained)
$e \cos \omega$	–	-0.003 ± 0.003
$e \sin \omega$	–	-0.027 ± 0.027
Velocity semi-amplitude K [m s^{-1}]	155 ± 7	156.3 ± 2.1

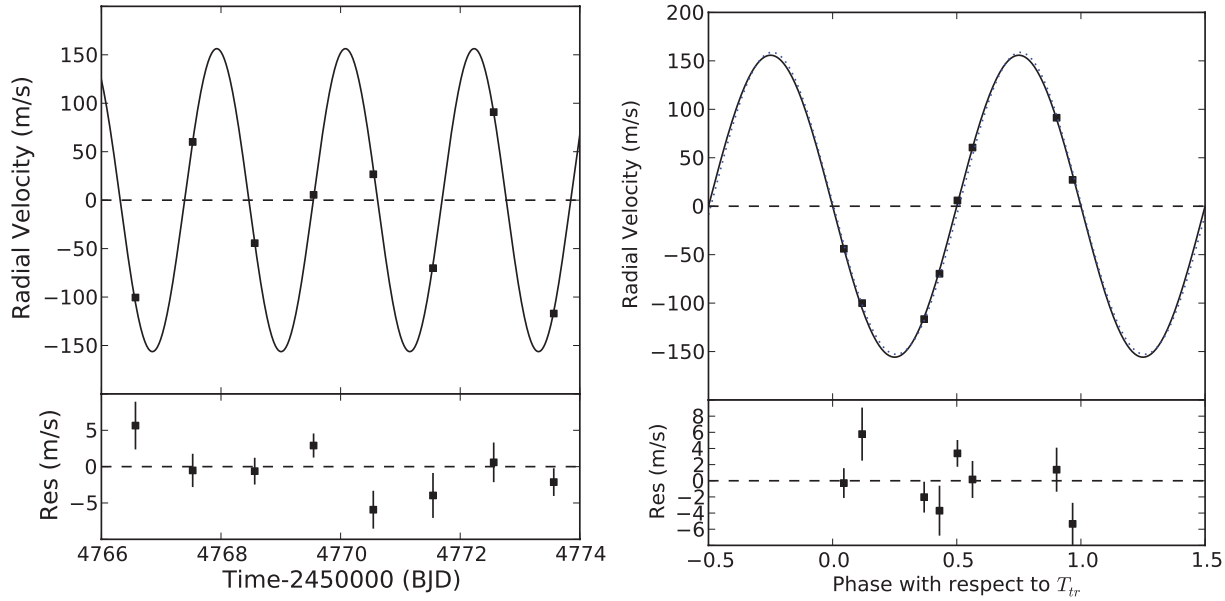

Figure 10. Plot showing our new HARPS RV data for WASP-2, plotted against time (left) and orbital phase with respect to $T_{\rm tr}$ (right). A circular orbit (solid line) and an orbit with the best-fitting eccentricity (dotted line, but almost undistinguishable from the circular solution since $e = 0.027$) are overplotted. The residuals relative to the circular orbit are shown in the bottom panel.

orbit, we obtained $\chi^2 = 13.88$ giving a value of $\mathrm{BIC_e} = 119.02$. We repeated these calculations to obtain a reduced χ^2 of unity for the eccentric orbit and estimated $\sigma_{\rm r} = 10.4\,\mathrm{m\,s^{-1}}$ for the SOPHIE data (the SOPHIE data set did not allow the MCMC to converge and yield a reduced χ^2 of unity with an eccentric orbit) and $\sigma_{\rm r} = 7.05\,\mathrm{m\,s^{-1}}$ for the HARPS data. For the circular orbit, we obtained $\chi^2 = 15.16$, and a value of $\mathrm{BIC_c} = 115.47$ and for the eccentric orbit, we obtained $\chi^2 = 13.49$ and a value of $\mathrm{BIC_e} = 119.47$. We therefore find that the circular orbit cannot be excluded for WASP-2. Furthermore, we exclude the possibility that $e > 0.1$.

Other planets

HD 189733b and HD 209458b are both on orbits that are compatible with a circular model: Laughlin et al. (2005) reported the 95 per cent limits on eccentricity for HD 209458b ($e < 0.042$) and we estimate the upper limit for HD 189733b from Triaud et al. (2009) assuming a Gaussian probability distribution, $e < 0.008$. In both cases, the eccentricity is strongly constrained by the timing of the secondary eclipse. No RV data were found for Kepler-5 in the literature or online, but we include the results of Kipping & Bakos (2011) in this study: Kepler-5b has an eccentricity of $e = 0.034^{+0.029}_{-0.018}$, with a 95 per cent upper limit of $e < 0.086$. We therefore classify Kepler-5b as having a circular orbit. We also omitted an analysis of the two-planet system HAT-P-13, choosing to estimate the 95 per cent limits on the orbital eccentricity of HAT-P-13b from the literature ($e < 0.022$) and classify this orbit as circular.

4.3 Planets on eccentric orbits

In contrast to Section 4.1, in this section, we confirm the eccentricities of 10 planets. We verify the eccentricities of CoRoT-9b, GJ-436b and HAT-P-2b as a test for our procedures and we also confirm the eccentricities of HAT-P-16b and WASP-14b, with the former being the planet on a short period orbit with the smallest confirmed eccentricity, and the latter being the planet with the shortest period orbit having a confirmed eccentricity. Finally we note the confirmed orbital eccentricities of CoRoT-10b, HAT-P-15b, HD 17156b, HD 80606b and XO-3b.

CoRoT-9

CoRoT-9b is a 0.84 M_j planet on a 95.3 d orbit around a G3 star ($V = 13.5$), first reported by Deeg et al. (2010), who found an eccentricity of $e = 0.11 \pm 0.04$. We used the 14 HARPS measurements from Deeg et al. (2010), setting $\tau = 1.5$ d and $\sigma_{\rm r} = 3.7\,\mathrm{m\,s^{-1}}$ to obtain a value of reduced χ^2 of unity for the circular orbit. We imposed the prior information from photometry $P = 95.2738(14)$ and $T_{\rm tr} = 2454\,603.3447(1)$ from Deeg et al. (2010) and obtained a value of $\chi^2_{\rm c} = 14.05$ and $\chi^2_{\rm e} = 7.90$. Using $N = 16$, $k_{\rm c} = 2$ and $k_{\rm e} = 4$, we obtain $\mathrm{BIC_c} = 106.17$ and $\mathrm{BIC_e} = 105.57$, which provides marginal support for an eccentric orbit at $e = 0.111 \pm 0.046$, with the 95 per cent limit at $e < 0.20$. We repeated the calculations, setting $\sigma_{\rm r} = 0\,\mathrm{m\,s^{-1}}$ since this results in a reduced χ^2 of less than unity for the eccentric orbit. This time, we obtained a value of $\chi^2_{\rm c} = 16.65$ and $\chi^2_{\rm e} = 9.63$. Using $N = 16$, $k_{\rm c} = 2$ and $k_{\rm e} = 4$, we obtain $\mathrm{BIC_c} = 105.66$ and $\mathrm{BIC_e} = 104.18$, which supports an eccentric orbit at $e = 0.111 \pm 0.039$.

GJ-436

GJ-436b is a 0.071 M_j planet on a 2.64 d eccentric orbit around an M2.5 star (V = 10.7), first reported by Butler et al. (2004). Deming et al. (2007) detected the secondary eclipse using *Spitzer*, placing a constraint on the secondary eclipse phase $\phi_{\rm occ} = 0.587 \pm 0.005$. This translates into $e\cos\omega = 0.1367 \pm 0.0012$, which we apply as a Bayesian prior in the calculation of our merit function.

We used the 59 HIRES measurements from Maness et al. (2007), setting $\tau = 1.5$ d and $\sigma_{\rm r} = 5.5\,\mathrm{m\,s^{-1}}$ to obtain a value of reduced χ^2 of unity for the circular orbit. We imposed the prior information from photometry $P = 2.643\,85(9)$ from Maness et al. (2007)and $T_{\rm tr} = 2454\,280.781\,49(16)$ from Deming et al. (2007) and obtained a value of $\chi^2_{\rm c} = 59.74$ and $\chi^2_{\rm e} = 38.86$. Using $N = 61$ (59 measurements and two priors from photometry) and $k_{\rm c} = 2$ for the circular orbit, we obtain $\mathrm{BIC_c} = 371.38$. Using $N = 62$ (59 measurements and three priors from photometry) and $k_{\rm e} = 3$ ($V_0, K, e\sin\omega$) for the eccentric

orbit, we obtain $BIC_e = 354.67$, which supports an eccentric orbit at $e = 0.157 \pm 0.024$, with the 95 per cent limit at $e < 0.21$. We repeated the calculations, setting $\sigma_r = 3.95\,m\,s^{-1}$ to obtain a reduced χ^2 of unity for the eccentric orbit. This time, we obtained a value of $\chi^2_c = 88.20$ and $\chi^2_e = 59.39$. We also obtain $BIC_c = 372.67$ and $BIC_e = 348.03$, which supports an eccentric orbit at $e = 0.153 \pm 0.017$, which is in agreement with Deming et al. (2007), who reported $e = 0.150 \pm 0.012$.

HAT-P-16

HAT-P-16b is a 4.19 M_j planet on a 2.78 d orbit around an F8 star (V = 10.7), first reported by Buchhave et al. (2010). The original authors found an eccentricity of $e = 0.036 \pm 0.004$. We re-analysed the seven high-resolution FIES measurements, 14 medium-resolution FIES measurements and six HIRES measurements, with two priors from photometry on the period and mid-transit time. We set $\tau = 1.5$ d for all instruments and set $\sigma_r = 115$, 185 and 28 $m\,s^{-1}$, respectively, for the three instruments to obtain a reduced χ^2 of unity for each individually. We then analysed them together using both a circular ($\chi^2 = 28.83$) and an eccentric orbit ($\chi^2 = 3.81$). Using $N = 29$, $k_c = 4$ and $k_e = 6$, we obtain $BIC_c = 314.74$ and $BIC_e = 296.45$, which supports an eccentric orbit at $e = 0.034 \pm 0.010$. Fig. 11 (left) shows the data from Buchhave et al. (2010), with a circular orbit overplotted with a solid line and an eccentric orbit with the dotted line. The residuals are plotted for the circular solution and they show a clear periodic signal.

We repeated the analysis, this time setting $\sigma_r = 0$ (reduced $\chi^2 = 0.62$, indicating over-fitting), 16 (reduced $\chi^2 = 33$) and 4.7 $m\,s^{-1}$, respectively, and separately for the three data sets (i.e. aiming for a reduced χ^2 of unity for each data set individually, with an eccentric orbit). We then analysed them together using both a circular ($\chi^2 = 347.86$) and an eccentric orbit ($\chi^2 = 44.62$). Using $N = 29$, $k_c = 4$ and $k_e = 6$, we obtain $BIC_c = 541.64$ and $BIC_e = 245.14$, which supports an eccentric orbit at $e = 0.034 \pm 0.003$. We thus confirm the eccentricity of HAT-P-16b, which means this is the planet with the smallest eccentricity that is reliably measured. This is in part helped by the fact that HAT-P-16b is a very massive planet, making the RV signal for an eccentric orbit very clear. Fig. 11 (right) shows the data from Buchhave et al. (2010) again, with an eccentric orbit overplotted with the dotted line.

WASP-14

WASP-14b is a 7.3 M_j planet on a 2.24 d orbit around an F5 star ($V = 9.8$), first reported by Joshi et al. (2009), who found an eccentricity of $e = 0.091 \pm 0.003$. Husnoo et al. (2011) confirmed the eccentricity of the orbit and updated the precise value to $e = 0.088 \pm 0.003$. This makes WASP-14b the planet that is closest to its host star but still has an eccentric orbit, taking the place from WASP-12b.

CoRoT-10, HAT-P-2, HAT-P-15, HD 17156, HD 80606 and XO-3

The orbits of the planets CoRoT-10b ($e = 0.110 \pm 0.039$), HAT-P-2b ($e = 0.517 \pm 0.003$), HAT-P-15b ($e = 0.190 \pm 0.019$), HD 17156b ($e = 0.677 \pm 0.003$), HD 80606b ($e = 0.934 \pm 0.001$) and XO-3b ($e = 0.287 \pm 0.005$) are clearly eccentric from existing literature (see e.g. Hébrard et al. 2008, 2010; Loeillet et al. 2008; Bonomo et al. 2010; Kovács et al. 2010; Nutzman et al. 2011, respectively).

4.4 Planets with orbits that have poorly constrained eccentricities

For 26 of the transiting planets that we attempted to place upper limits on their eccentricities, we obtained limits that were larger than 0.1. We considered these eccentricities to be poorly determined. We discuss the cases of HAT-P-4b, WASP-7, XO-2b and Kepler-4b below.

HAT-P-4 (new SOPHIE data)

HAT-P-4b is a 0.68 M_j planet on a 3.06 d orbit around an F star (V=11.2), first reported by Kovacs et al. (2007). We use 13 new SOPHIE RV measurements and the nine HIRES measurements in Kovacs et al. (2007) to work out the orbital parameters of HAT-P-4b. We impose the period $P = 3.056\,536(57)$ d and mid-transit time $T_{tr} = 2454\,248.8716(6)$ BJD as given from photometry in Kovacs et al. (2007). We set $\tau = 1.5$ d and $\sigma_r = 3.35\,m\,s^{-1}$ for SOPHIE

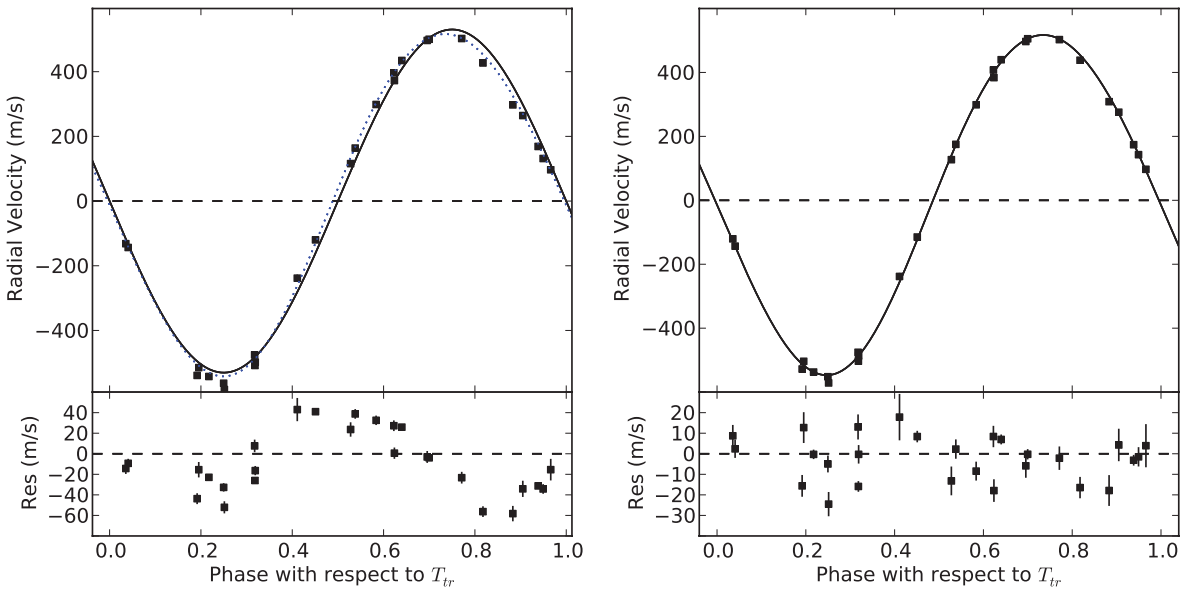

Figure 11. Plot showing RV data from Buchhave et al. (2010) for HAT-P-16, plotted against orbital phase with respect to T_{tr}. Left: a circular orbit is overplotted with a solid line and an eccentric orbit ($e = 0.034$) is plotted with a dotted line. The bottom panel shows the residuals for a circular orbit: these show a clear periodic signal, indicating the possibility of an eccentric orbit. Right: an eccentric orbit ($e = 0.034$) is plotted with a solid line. The residuals are shown for the eccentric orbit.

Table 16. System parameters for HAT-P-4. Left: Kovacs et al. (2007). Right: results from our new SOPHIE RV data and the original HIRES data. Median values for V_0 and K are quoted for the circular orbits, as well as 68.3 per cent confidence limits obtained from the eccentric solution. The 95 per cent upper limit on eccentricity is also given.

Parameter	HIRES, Kovacs et al. (2007)	HIRES+SOPHIE, This Work
Centre-of-mass velocity V_0 [m s^{-1}]	12.1 ± 0.9	20.3 ± 2.6 (HIRES), −1402.0 ± 4.0 (SOPHIE)
Orbital eccentricity e	0 (adopted)	0.064 ± 0.028, $e < 0.11$
Argument of periastron ω [^{o}]	0 (unconstrained)	0 (unconstrained)
$e \cos \omega$	–	−0.018±0.012
$e \sin \omega$	–	−0.061 ± 0.027
Velocity semi-amplitude K [m s^{-1}]	81.1 ± 1.9	81.3 ± 2.6

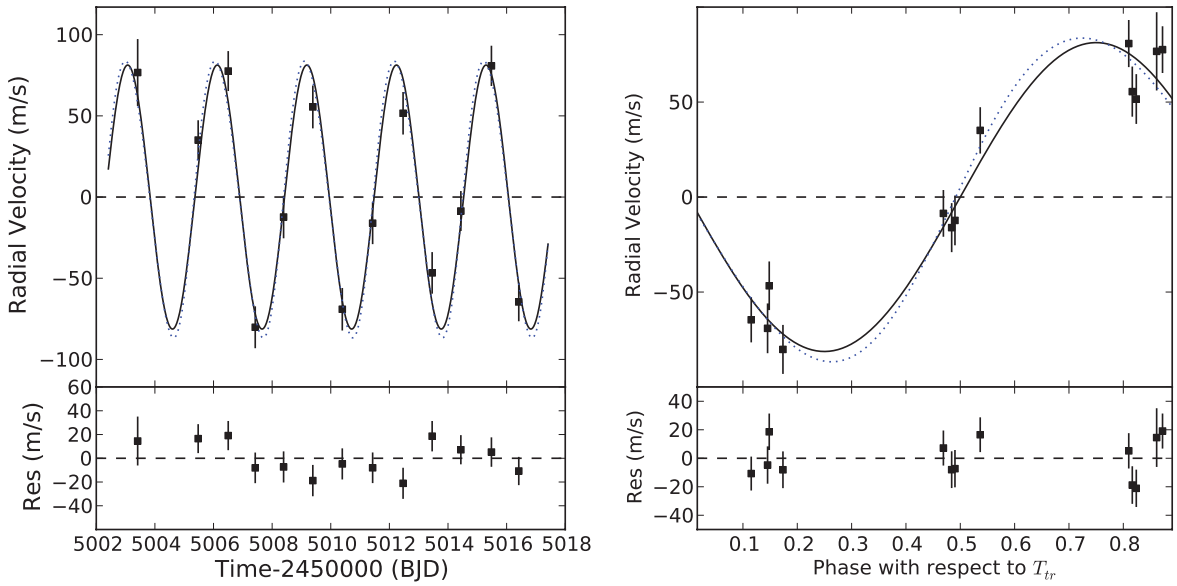

Figure 12. Plot showing our new HARPS RV data for HAT-P-4, plotted against time (left) and orbital phase with respect to $T_{\rm tr}$ (right). A circular orbit (solid line) and an orbit with the best-fitting eccentricity (dotted line, $e = 0.064$) are overplotted. The residuals relative to the circular orbit are shown in the bottom panel.

and $\sigma_{\rm r} = 3.75$m s^{-1} for HIRES to obtain a reduced χ^2 of unity for each data set separately for the best-fitting circular orbit. We used 22 measurements in all, and count the two constraints from photometry as two additional data points ($N = 24$), and used $k = 3$ for the circular orbit (two V_0, one for each data set, and the semi-amplitude K). We repeated this analysis with an eccentric orbit $k = 5$ (3 degrees of freedom for the circular orbit, and 2 additional degrees of freedom for the eccentricity, $e \cos \omega$ and $e \sin \omega$). The orbital parameters are given in Table 16, and the RV data set is plotted in Fig. 12, with residuals shown for a circular orbit. The figure also shows models of a circular and an eccentric orbit (with $e = 0.064$). For the circular orbit, we obtained $\chi^2 = 22.05$, giving a value of BIC$_{\rm c} = 161.96$ and for the eccentric orbit, we obtained $\chi^2 = 16.77$, giving a value of BIC$_{\rm e} = 163.04$. We repeated these calculations by setting $\tau = 1.5d$, $\sigma_{\rm r} = 1.81$ m s^{-1} for HIRES, and kept $\sigma_{\rm r} = 3.35$ m s^{-1} for SOPHIE, since we were unable to determine a value of $\sigma_{\rm r}$ that would allow the MCMC chain to converge and lead to a χ^2 of unity for an eccentric orbit. This time, we obtained $\chi^2 = 25.88$ for the circular orbit, giving a value of BIC$_{\rm c} = 161.96$ and for the eccentric orbit, we obtained $\chi^2 = 20.05$ giving a value of BIC$_{\rm e} = 162.49$. We find that the circular orbit cannot be excluded for HAT-P-4b, but because the eccentricity is $e = 0.064 \pm 0.028$ with an upper limit of $e < 0.11$, which is above 0.1, we classify HAT-P-4b as having a poorly constrained eccentricity.

WASP-7 (new HARPS data)

WASP-7b is a 1.0 M_j planet on a 4.95 d orbit around an F5 star (V = 9.5), first reported by Hellier et al. (2009b). We analysed our 11 new HARPS measurements for WASP-7 as well as 11 measurements from Hellier et al. (2009b) using CORALIE, and used the photometric constraints on the orbital period $P = 4.954\,658(55)$ and mid-transit time $T_{\rm tr} = 2453\,985.0149(12)$ from the same paper. For both instruments, we set $\tau = 1.5$ d and for CORALIE, we set $\sigma_{\rm r} = 28.3$ m s^{-1} while for HARPS, we set $\sigma_{\rm r} = 210$ m s^{-1} in order to get a value of reduced χ^2 equal to unity for the circular orbit. We performed the MCMC analysis twice: the first time fitting for the systemic velocity v_0 and semi-amplitude K, and the second time adding two parameters $e \cos \omega$ and $e \sin \omega$ to allow for an eccentric orbit. The best-fitting parameters are given in Table 17. We plot the RV data against time (Fig. 13, left) and phase (Fig. 13, right). When the residuals for a circular orbit are plotted, a scatter of about 30 m s^{-1} is clearly seen, which is much larger than the median uncertainties of $\sigma = 2.21$ m s^{-1} on the RV measurements. This is similar to that found by Hellier et al. (2009b) from their CORALIE

Table 17. System parameters for WASP-7. Left: Hellier et al. (2009b). Right: results from our HARPS radial velocity data. Median values for V_0 and K are quoted for the circular orbits, as well as 68.3 per cent confidence limits obtained from the eccentric solution (see section 'Analysis').

Parameter	Hellier et al. (2009b)	HARPS, This Work
Centre-of-mass velocity V_0 [m s^{-1}]	-29850.6 ± 1.7	-29455 ± 103
Orbital eccentricity e	0 (adopted)	0.103 ± 0.061 (<0.25)
Argument of periastron ω [^{o}]	0 (unconstrained)	0 (unconstrained)
$e \cos \omega$	–	0.021 ± 0.068
$e \sin \omega$	–	0.101 ± 0.074
Velocity semi-amplitude K [m s^{-1}]	97 ± 13	96 ± 14

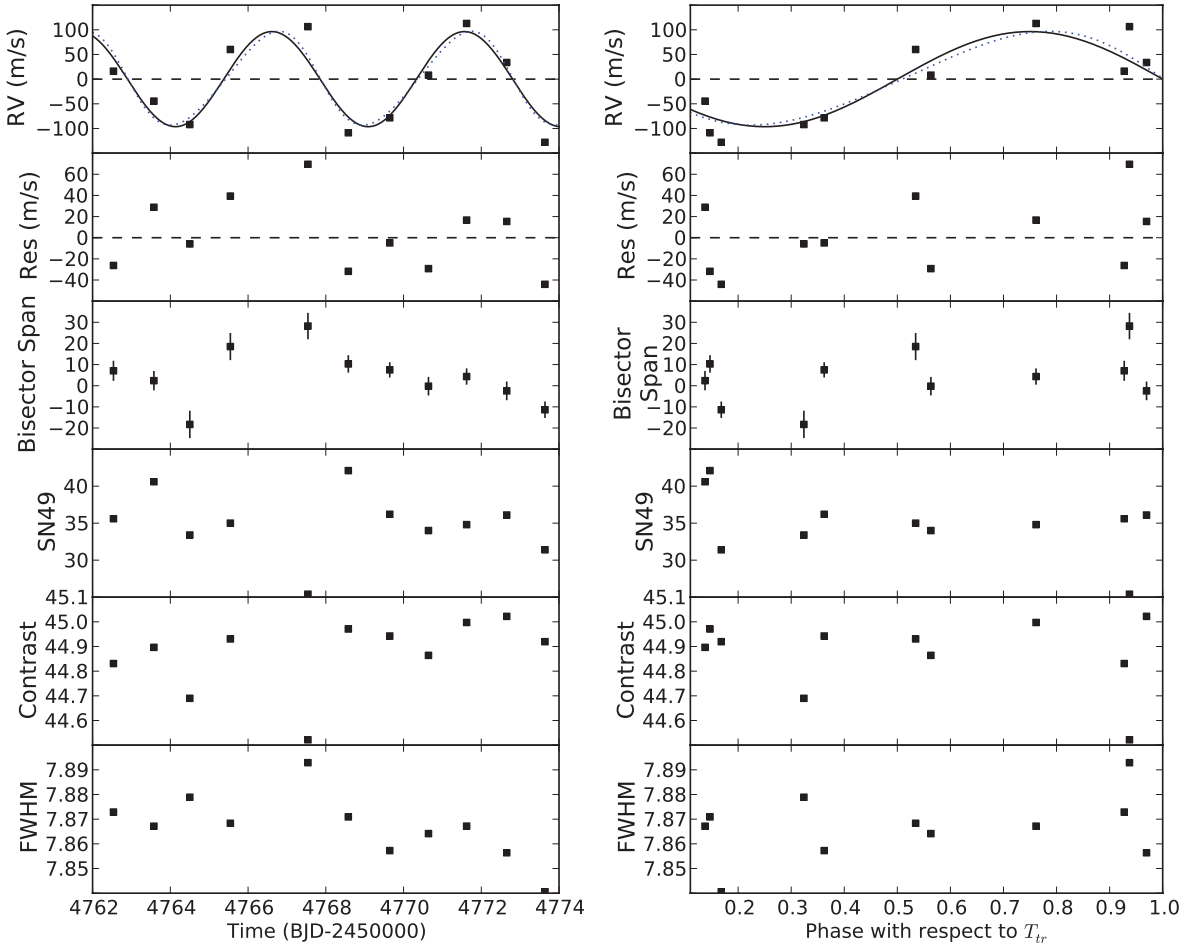

Figure 13. HARPS measurements of WASP-7 plotted against time (left) and phase with respect to the mid-transit time $T_{\rm tr}$ (right). In each case, a solid line is overplotted to represent a circular orbit and the residuals are plotted for this circular orbit. It is clear that a signal is present in the residuals (see text). An eccentric orbit with the best-fitting value of $e = 0.103$ is overplotted in both panels with a dotted line, but it is almost indistinguishable from the circular solution at this scale.

data. An eccentric orbit does not reduce the scatter. The value of χ^2 for the circular orbit is 22.37 and that for an eccentric orbit is 18.11. This leads to a value of $\mathrm{BIC_c} = 250.62$ and $\mathrm{BIC_e} = 252.72$, respectively, for 22 measurements, two constraints from photometry and three and five free parameters, respectively (Keplerian orbits, but with two V_0 to account for a possible offset between the two instruments). This shows that the circular orbit is still preferred, and an eccentric orbit does not explain the scatter. We repeated this using $\sigma_{\rm r} = 33.8\,\mathrm{m\,s^{-1}}$ for CORALIE while for HARPS, we set $\sigma_{\rm r} = 158.5\,\mathrm{m\,s^{-1}}$ in order to get a value of reduced χ^2 equal to unity for the eccentric orbit. We performed the MCMC analysis both for a circular and an eccentric orbit. The value of χ^2 for the circular orbit is 146.95 and that for an eccentric orbit is 146.86. This leads to a value of $\mathrm{BIC_c} = 367.47$ and $\mathrm{BIC_e} = 373.91$, respectively, for 22 measurements, two constraints from photometry and three and five free parameters, respectively (Keplerian orbits, but with two V_0 to account for a possible offset between the two instruments). This shows that the circular orbit is still preferred, and an eccentric orbit does not explain the scatter. WASP-7 is an F5V star, with a temperature of $T_{\rm eff} = 6400 \pm 100$ K. Despite the result of the

original paper that WASP-7 is not chromospherically active above the 0.02 mag level, Lagrange et al. (2009) found evidence for other F5V stars showing RV variability with a scatter at this level, for example HD 111998, HD 197692 or HD 205289, with scatters of 40 m s^{-1} 30 m s^{-1} and 29 m s^{-1}, respectively. Our derived value of eccentricity is $e = 0.103 \pm 0.061$, with the 95 per cent upper limit at $e < 0.25$. We therefore classify the eccentricity of the orbit of WASP-7b as poorly constrained

In Fig. 13, we have also plotted the bisector span, the signal-to-noise ratio at the order of 49, the contrast and full width at half-maximum for the cross-correlation function against the same time axis. The large scatter in RV residuals can be seen to be correlated with both the bisector span and the full width at half-maximum of the cross-correlation function.

XO-2 (new SOPHIE data)

XO-2 is a 0.6 M_j planet on a 2.62 d orbit around a K0 star (V = 11.2), first reported by Burke et al. (2007). We use nine new SOPHIE RV measurements and the 10 HJS measurements in Burke et al. (2007) to work out the orbital parameters of XO-2. We impose the period $P = 2.615\,8640(21)$ d and mid-transit time $T_{\rm tr} = 2454\,466.884\,67(17)$ BJD as given from photometry in Fernandez et al. (2009). We set $\tau = 1.5$ d and $\sigma_{\rm r} = 5.3$ m s^{-1} for SOPHIE and $\sigma_{\rm r} = 0$ m s^{-1} for HJS (because the HJS data alone, with a circular orbit, yield a reduced χ^2 of 0.78, indicating overfitting) to obtain a reduced χ^2 of unity for the best-fitting circular orbit. We used 19 measurements in all, and count the two constraints from photometry as two additional data points ($N = 21$), and used $k = 3$ for the circular orbit (two V_0, one for each data set, and the semi-amplitude K). We repeated this analysis with an eccentric orbit $k = 5$ (2 degrees of freedom for the circular orbit, and 2 additional degrees of freedom for the eccentricity, $e\cos\omega$ and $e\sin\omega$). The orbital parameters are given in Table 18, and the RV data set is plotted in Fig. 14, with residuals shown for a circular orbit. The figure also shows models of a circular and an eccentric orbit (with $e = 0.064$). For the circular orbit, we obtained $\chi^2 = 19.65$, giving a value of BIC$_{\rm c} = 165.55$ and for the eccentric orbit, we obtained $\chi^2 = 17.57$ giving a value of BIC$_{\rm e} = 169.55$. We repeated the calculations using $\sigma_{\rm r} = 7.05$ m s^{-1} for SOPHIE and $\sigma_{\rm r} = 0$ m s^{-1} for HJS (because the HJS data alone, with an eccentric orbit, yield a reduced χ^2 of 0.56, indicating overfitting) to obtain a reduced χ^2 of unity for the best-fitting eccentric orbit. For the circular orbit, we obtained $\chi^2 = 18.02$, giving a value of BIC$_{\rm c} = 165.21$ and for the eccentric orbit, we obtained $\chi^2 = 16.01$ giving a value of BIC$_{\rm e} = 169.29$. In both cases, i.e. using the optimal value of $\sigma_{\rm r}$ for a circular orbit and using the optimal value of $\sigma_{\rm r}$ for an eccentric orbit, a circular orbit is favoured. The 95 per cent upper limit is $e < 0.14$, which is above 0.1, so we classify the orbital eccentricity of XO-2 as poorly constrained.

Kepler-4

Kepler-4b has a derived eccentricity of $e = 0.25^{+0.11}_{-0.12}$, with a 95 per cent upper limit of $e < 0.43$ (Kipping & Bakos 2011), so we classify it as 'poorly constrained eccentricity'.

Other objects

For the eight objects CoRoT-6, HAT-P-1, HAT-P-3, HAT-P-6, HD 149026, Kepler-6, WASP-10 and WASP-21, we found the BIC$_{\rm e}$ for an eccentric orbit was smaller than the BIC$_{\rm c}$ for a circular orbit if we assume a $\sigma_{\rm r}$ that yields a reduced χ^2 of unity for an eccentric orbit, whereas the BIC$_{\rm c}$ for a circular orbit was smaller than the BIC$_{\rm e}$ for an eccentric orbit if we assume a $\sigma_{\rm r}$ that yields a reduced χ^2 of unity for a circular orbit. This suggests that the current RV data sets do not constrain the orbit enough for us to detect a finite eccentricity. We have already discussed the case of WASP-10b in Section 4.1.

4.5 Additional planetary systems

In addition to the 64 planets considered so far, we now include three additional planets on eccentric orbits, 11 planets on orbits where $e > 0.1$ is excluded at the 95 per cent level and two brown dwarves. The additional planets on eccentric orbits are HAT-P-17b (Howard et al. 2010, $e = 0.346 \pm 0.007$), HAT-P-21b (Bakos et al. 2011, $e = 0.228 \pm 0.016$) and HAT-P-31b (Kipping et al. 2011, $e = 0.245 \pm 0.005$). The additional planets on orbits that are consistent with circular are:

CoRoT-18b ($e < 0.08$ at 3σ, Hébrard et al. 2011),
HAT-P-20b ($e < 0.023$, estimated from Bakos et al. 2011),
HAT-P-22b ($e < 0.031$, estimated from Bakos et al. 2011),
HAT-P-25b ($e < 0.068$, estimated from Quinn et al. 2012),
HAT-P-30b ($e < 0.074$, estimated from Johnson et al. 2011),
WASP-23b ($e < 0.062$ at 3σ, Triaud et al. 2011),
WASP-34b ($e < 0.058$, estimated from Smalley et al. 2011),
WASP-43b ($e < 0.04$ at 3σ, Hellier et al. 2011),
WASP-45b ($e < 0.095$, Anderson et al. 2011),
WASP-46b ($e < 0.065$, Anderson et al. 2011) and
τ Boötis b ($e < 0.045$, estimated from Butler et al. 2006).

The two brown dwarves are OGLE-TR-122b (Pont et al. 2005a, $e = 0.205 \pm 0.008$) and OGLE-TR-123b (Pont et al. 2005b, $e = 0$). In addition to the above, we also consider the case of WASP-38 (Barros et al. 2011), which has an eccentricity of $e = 0.031 \pm 0.005$, indicating it is in the process of circularization, just like WASP-14 and HAT-P-16.

Table 18. System parameters for XO-2. Left: Burke et al. (2007). Right: results from our SOPHIE RV data. Median values for V_0 and K are quoted for the circular orbits, as well as 68.3 per cent confidence limits obtained from the eccentric solution. The 95 per cent upper limit on eccentricity is also given.

Parameter	HJS, Burke et al. (2007)	HJS, SOPHIE, This Work
Centre-of-mass velocity V_0 [m s^{-1}]	–	-1.3 ± 6.3 (HJS), 46860.1 ± 4.1 (SOPHIE)
Orbital eccentricity e	0 (adopted)	0.064 ± 0.041 ($e < 0.14$)
Argument of periastron ω [^{o}]	0 (unconstrained)	0 (unconstrained)
$e\cos\omega$	–	0.007 ± 0.017
$e\sin\omega$	–	-0.063 ± 0.047
Velocity semi-amplitude K [m s^{-1}]	85 ± 8	98.0 ± 4.0

Table 19. the objects that we considered in this study. We have included the fifth column to show if the object is on a circular orbit ('C', i.e. circular according to the BIC test and 95 per cent limit on e is less that 0.1), 'E', for objects that are on eccentric orbits (either determined to be eccentric using the BIC test, or the orbit is clearly eccentric from the RV plot), or 'P', for objects which we fail to place any useful constraints on the eccentricity (i.e. the 95 per cent limit on e is larger than 0.1), or it is unclear from model selection whether the orbit is circular or eccentric.

Name	Eccentricity (literature)	Eccentricity (this work)	95 per cent limit	E	$M_{\rm p}(M_j)$ (This Work)
CoRoT-1b	–	0.006 ± 0.012	(< 0.042)	C	1.06 ± 0.14
CoRoT-2b	–	0.036 ± 0.033	(< 0.10)	P	3.14 ± 0.17
CoRoT-3b	$0.008^{+0.015}_{-0.005}$	0.012 ± 0.01	(< 0.039)	C	21.61 ± 1.2
CoRoT-4b	0 ± 0.1	0.27 ± 0.15	(< 0.48)	P	0.659 ± 0.079
CoRoT-5b	$0.09^{+0.09}_{-0.04}$	0.086 ± 0.07	(< 0.26)	P	0.488 ± 0.032
CoRoT-6b	<0.1	0.18 ± 0.12	(< 0.41)	P	2.92 ± 0.30
CoRoT-9b	0.11 ± 0.04	0.11 ± 0.039	(< 0.20)	E	0.839 ± 0.070
CoRoT-10b	0.53 ± 0.04	0.53 ± 0.04	–	E	2.75 ± 0.16
GJ-436b	0.150 ± 0.012	0.153 ± 0.017	–	E	0.069 ± 0.006
GJ-1214b	<0.27 (95 per cent)	0.12 ± 0.09	(< 0.34)	P	0.020 ± 0.003
HAT-P-1b	<0.067 (99 per cent)	0.048 ± 0.021	(< 0.087)	P	0.514 ± 0.038
HAT-P-2b	0.517 ± 0.003	0.517 ± 0.003	–	E	8.76 ± 0.45
HAT-P-3b	–	0.1 ± 0.05	(< 0.20)	P	0.58 ± 0.17
HAT-P-4b	–	0.063 ± 0.028	(< 0.107)	P	0.677 ± 0.049
HAT-P-5b	–	0.053 ± 0.061	(< 0.24)	P	1.09 ± 0.11
HAT-P-6b	–	0.047 ± 0.017	(< 0.078)	P	1.031 ± 0.053
HAT-P-7b	<0.039 (99 per cent)	0.014 ± 0.01	(< 0.037)	C	1.775 ± 0.070
HAT-P-8b	–	0.011 ± 0.019	(< 0.064)	C	1.340 ± 0.051
HAT-P-9b	–	0.157 ± 0.099	(< 0.40)	P	0.767 ± 0.10
HAT-P-11b	0.198 ± 0.046	0.28 ± 0.32	(< 0.80)	P	0.055 ± 0.022
HAT-P-12b	–	0.071 ± 0.053	(< 0.22)	P	0.187 ± 0.033
HAT-P-13b	$0.014^{+0.005}_{-0.004}$	0.014 ± 0.005	(< 0.022)	C	0.855 ± 0.046
HAT-P-14b	0.107 ± 0.013	0.11 ± 0.04	(< 0.18)	P	2.23 ± 0.12
HAT-P-15b	0.190 ± 0.019	0.19 ± 0.019	–	E	1.949 ± 0.077
HAT-P-16b	0.036 ± 0.004	0.034 ± 0.003	(< 0.039)	ES	4.20 ± 0.11
HD 17156b	0.677 ± 0.003	0.675 ± 0.004	–	E	3.223 ± 0.087
HD 80606b	0.934 ± 0.001	0.933 ± 0.001	–	E	3.99 ± 0.33
HD 149026b	–	0.121 ± 0.053	(< 0.21)	P	0.354 ± 0.031
HD 189733b	$0.004^{+0.003}_{-0.002}$	0.004 ± 0.003	(< 0.0080)	C	1.139 ± 0.035
HD 209458b	0.014 ± 0.009	0.014 ± 0.009	(< 0.042)	C	0.677 ± 0.033
Kepler-4b	$0.25^{+0.11}_{-0.12}$ (<0.43)	0.25 ± 0.12	(< 0.43)	P	0.077 ± 0.028
Kepler-5b	$0.034^{+0.029}_{-0.018}$ (<0.086)	0.034 ± 0.029	(< 0.086)	C	2.120 ± 0.079
Kepler-6b	$0.056^{+0.044}_{-0.028}$ (<0.13)	0.057 ± 0.026	(< 0.12)	P	0.659 ± 0.038
Kepler-7b	$0.102^{+0.104}_{-0.047}$ (<0.31)	0.065 ± 0.045	(< 0.19)	P	0.439 ± 0.044
Kepler-8b	$0.35^{+0.15}_{-0.11}$ (<0.59)	0.011 ± 0.24	(< 0.39)	P	0.57 ± 0.11
TrES-1b	–	0.019 ± 0.054	(< 0.21)	P	0.757 ± 0.061
TrES-2b	–	0.023 ± 0.014	(< 0.051)	C	1.195 ± 0.063
TrES-3b	–	0.066 ± 0.048	(< 0.16)	P	1.86 ± 0.12
TrES-4b	–	0.21 ± 0.21	(< 0.66)	P	0.93 ± 0.17
WASP-1b	–	0.19 ± 0.22	(< 0.65)	P	0.89 ± 0.15
WASP-2b	–	0.027 ± 0.023	(< 0.072)	C	0.852 ± 0.080
WASP-3b	–	0.009 ± 0.013	(< 0.048)	C	1.99 ± 0.13
WASP-4b	–	0.005 ± 0.003	(< 0.011)	C	1.205 ± 0.044
WASP-5b	$0.038^{+0.026}_{-0.018}$	0.012 ± 0.007	(< 0.026)	C	1.571 ± 0.063
WASP-6b	$0.054^{+0.018}_{-0.015}$	0.041 ± 0.019	(< 0.075)	C	0.480 ± 0.038
WASP-7b	–	0.074 ± 0.063	(< 0.23)	P	1.07 ± 0.16
WASP-10b	$0.057^{+0.014}_{-0.004}$	0.052 ± 0.031	(< 0.11)	P	3.15 ± 0.12
WASP-11b	–	0.091 ± 0.054	(< 0.21)	P	0.470 ± 0.035
WASP-12b	0.049 ± 0.015	0.018 ± 0.018	(< 0.05)	C	1.48 ± 0.14
WASP-13b	–	0.14 ± 0.1	(< 0.32)	P	0.458 ± 0.064
WASP-14b	0.091 ± 0.004	0.088 ± 0.003	(< 0.090)	ES	7.26 ± 0.59
WASP-15b	–	0.056 ± 0.048	(< 0.17)	P	0.548 ± 0.059
WASP-16b	–	0.009 ± 0.012	(< 0.047)	C	0.846 ± 0.072
WASP-17b	$0.129^{+0.106}_{-0.068}$	0.121 ± 0.093	(< 0.32)	P	0.487 ± 0.062

Table 19 – *continued*

Name	Eccentricity (literature)	Eccentricity (this work)	95 per cent limit	E	$M_p(M_j)$ (This Work)
WASP-18b	0.009 ± 0.001	0.007 ± 0.005	(< 0.018)	C	10.16 ± 0.87
WASP-19b	0.02 ± 0.01	0.011 ± 0.013	(< 0.047)	C	1.15 ± 0.10
WASP-21b	–	0.048 ± 0.024	(< 0.11)	P	0.308 ± 0.018
WASP-22b	0.023 ± 0.012	0.022 ± 0.016	(< 0.057)	C	0.56 ± 0.13
WASP-26b	–	0.033 ± 0.025	(< 0.086)	C	1.018 ± 0.034
XO-1b	–	0.042 ± 0.088	(< 0.30)	P	0.911 ± 0.088
XO-2b	–	0.064 ± 0.041	(< 0.14)	P	0.652 ± 0.032
XO-3b	0.287 ± 0.005	0.287 ± 0.005	–	E	11.81 ± 0.53
XO-4b	–	0.28 ± 0.15	(< 0.50)	P	1.56 ± 0.30
XO-5b	–	0.01 ± 0.01	(< 0.036)	C	1.065 ± 0.036

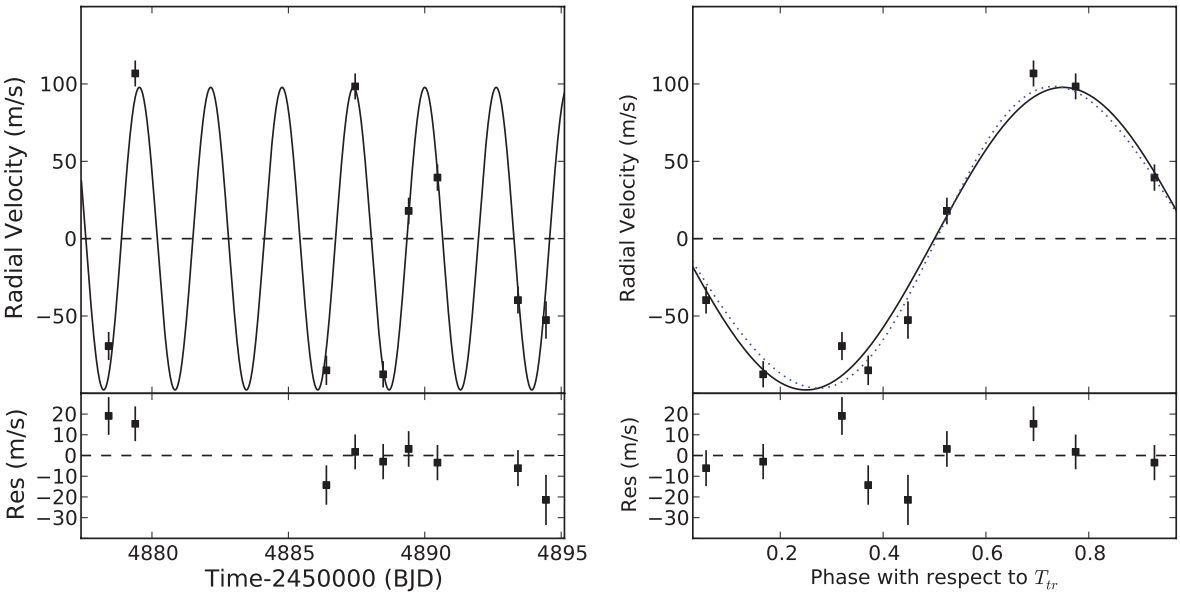

Figure 14. Plot showing our new SOPHIE RV data for XO-2, plotted against orbital phase with respect to $T_{\rm tr}$. A circular orbit (solid line) and an orbit with the best-fitting eccentricity (dotted line, but almost undistinguishable from the circular solution since $e = nnnn$) are overplotted. The residuals relative to the circular orbit are shown in the bottom panel.

5 DISCUSSION

5.1 The mass–period plane

We now discuss the results of the previous sections in the context of tidal evolution in hot Jupiters. Fig. 15 shows a plot of the mass ratio $M_{\rm p}/M_{\rm s}$ against orbital period for transiting planets with orbital period $P < 20$ d. The empty symbols represent orbits that are consistent with circular, and the black symbols represent eccentric orbits, whereas grey symbols represent objects with small ($e < 0.1$), but significant eccentricities. The circles represent the G dwarfs and the squares represent F dwarfs. It appears that the low mass hot Jupiters on orbits that are consistent with circular around G dwarfs migrate inwards until they stop at a minimum period for a given mass, conglomerating on the mass–period relation of Mazeh et al. (2005). In this case, the heavier planets can move in further before they are stopped. Planets heavier than about 1.2 M_j can migrate inwards and raise tides on the star, leading to a spin-up of the host star, and even synchronization in some cases where enough angular momentum can be transferred from the orbital motion into the stellar rotation. In cases where the planetary angular momentum is insufficient, the process can lead to a run-away migration until the planet is destroyed inside the star.

The Roche limit for a planet is defined by $R_{\rm p} = 0.462 a_R (M_{\rm p}/M_{\rm s})^{-3}$. If we write the stopping distance $a = \alpha a_R$, Ford & Rasio (2006) argued that slow migration on quasi-circular orbits would result in a value of $\alpha = 1$, with the only surviving planets being those that stop at their Roche limit. On the other hand, if the planets were brought in on an eccentric orbit (e.g. dynamical interactions within a system or capture from interstellar space), and then circularized by tidal interaction, the value of α should be two. In Fig. 15, the dashed line shows this case, with $\alpha = 2$. This does not appear to be a very good fit for the hot Jupiters that are on orbits consistent with circular. The dotted lines show the range $\alpha = 2.5$–4.5. As mentioned in Pont et al. (2011), this larger value of α could indicate the planets had larger radii at the time their orbits were circularized. Subsequent thermal evolution of the planets would have shrunk them (e.g. Baraffe et al. 2004), leaving them further out from their current Roche limits.

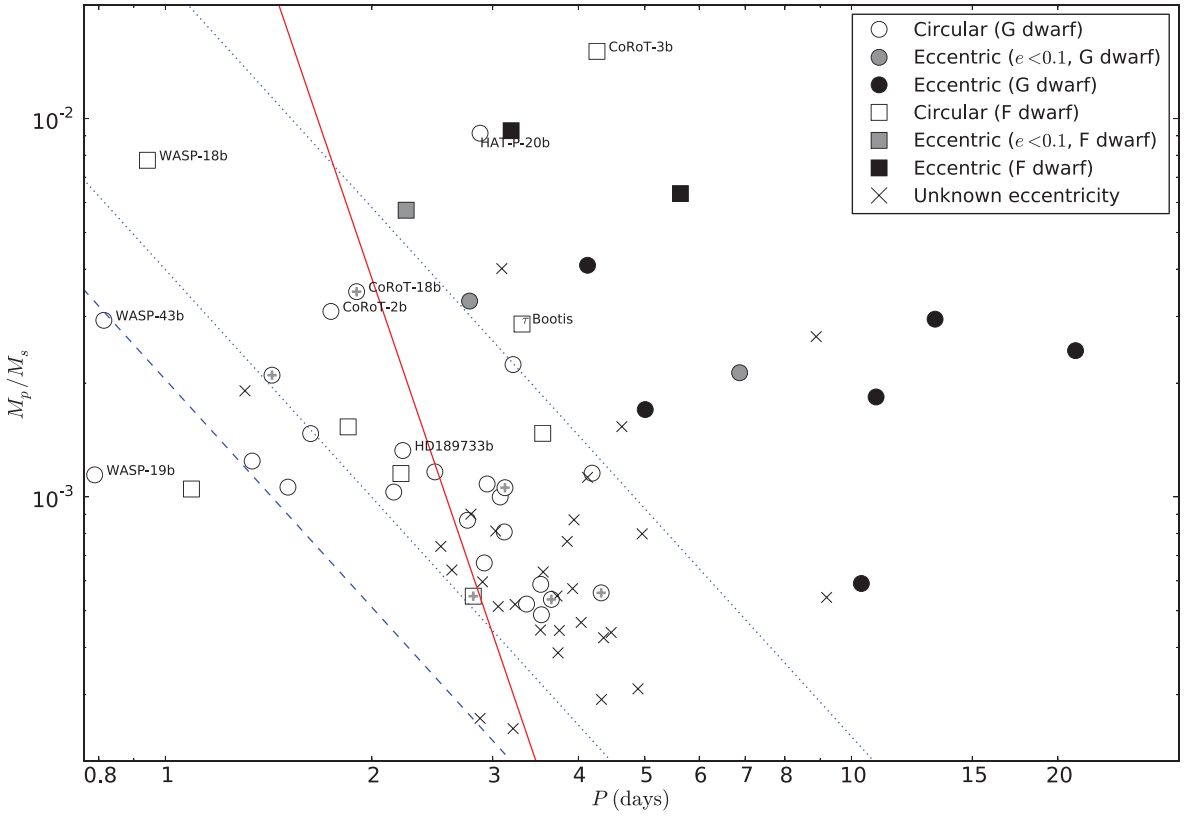

Figure 15. Plot showing the mass ratio v/s period plane, for transiting planets with orbital period $P < 20$ d. The low-mass hot Jupiters on orbits that are consistent with circular around G dwarfs migrate inwards until they stop at a minimum period for a given mass, conglomerating on the mass–period relation of Mazeh et al. (2005). The heavier planets can move in towards the star, and synchronize their rotations, as CoRoT-3b and τ Boötis b did, or if they lack the angular momentum to synchronize the star, they can continue migrating inwards towards their destruction, as WASP-18b appears to be doing. The labelled symbols (except for WASP-18b) represent objects on orbits that are consistent with circular where the host star rotation is significantly faster than the expected rotation from the isochrones of Strassmeier & Hall (1988). Five objects have been marked with a '+' symbol to mark objects with upper limits greater than $e < 0.05$ that are described in Section 4.5. The dashed line represents $\alpha = 2$ for $R_p = 1.2R_j$, while the dotted lines represent a value in the range $\alpha = 2.5$–4.5 in the equation $a = \alpha a_R$ (see text). The solid line represents a circularization isochrone at 1 Gyr for tides in the planet alone.

5.2 Circularization time-scales

The process of tidal circularization, spin–orbit alignment and synchronization is expected to occur roughly in this order, and over a similar time-scale. For close-in systems, this time-scale is expected to be small compared to the lifetime of the system. Hut (1981) derived equations for the tidal evolution due to the equilibrium tide using the assumption of weak friction, and constant time-lag Δt. Leconte et al. (2010) re-visited this model and showed that the orbital eccentricity evolves according to

$$\frac{1}{e}\frac{\mathrm{d}e}{\mathrm{d}t} = 11\frac{a}{GM_sM_p}\left\{K_p\left[\Omega_e(e)x_p\frac{\omega_p}{n} - \frac{18}{11}N_e(e)\right] + K_s\left[\Omega_e(e)x_s\frac{\omega_s}{n} - \frac{18}{11}N_e(e)\right]\right\}, \quad (11)$$

where $\Omega_e(e)$ and $N_e(e)$ are functions of e and approximately equal to unity for small e; x_p and x_s are the cosines of the angle between the orbital plane and the planet and stellar equators, respectively. ω_p and ω_s are the angular frequencies of rotation of the planet and star, and the two terms

$$K_p = \frac{3}{2}k_{2,p}\Delta t_p\left(\frac{GM_p^2}{R_p}\right)\left(\frac{M_s}{M_p}\right)^2\left(\frac{R_p}{a}\right)^6 n^2 \quad (12)$$

and

$$K_s = \frac{3}{2}k_{2,s}\Delta t_s\left(\frac{GM_s^2}{R_s}\right)\left(\frac{M_p}{M_s}\right)^2\left(\frac{R_s}{a}\right)^6 n^2 \quad (13)$$

describe the effect of tides on the planet by the star, and vice versa, respectively. n is the mean orbital motion and the semi-major axis is denoted by a. Under the assumption of a constant-time delay between the exciting tidal potential and the response of the equilibrium tide in the relevant body, $k_{2,p}\Delta t_p$ and $k_{2,s}\Delta t_s$ are constants where k_2 are the potential Love numbers of degree 2 and Δt are the constant time lags in each of the two bodies.

We now consider two limits, first the case where only the tides in the planet dominate, and then the case where only tides in the star dominate. When tides in the planet dominate, $K_s \sim 0$ so that we obtain a time-scale

$$\tau_p = -\left(\frac{1}{e}\frac{\mathrm{d}e}{\mathrm{d}t}\right)^{-1} = \frac{2}{21G}\frac{1}{k_{2,p}\Delta t_p}\frac{M_p}{M_s^2}\frac{a^8}{R_p^5}, \quad (14)$$

where we have assumed that $\Omega_e = N_e \approx 1$, i.e. the equation is valid to lowest order in e; $\omega_p/n \sim 1$, i.e. synchronization of the planetary rotation with the orbit and $x_p \sim 1$, i.e. the planet's equator coincides with the orbital plane. A similar equation can be written for tides in the star, even though ω_s/n is not typically unity. As long as $\omega_s/n <$ 18/11, for small e, the effect of tides in the star will lead to a decrease

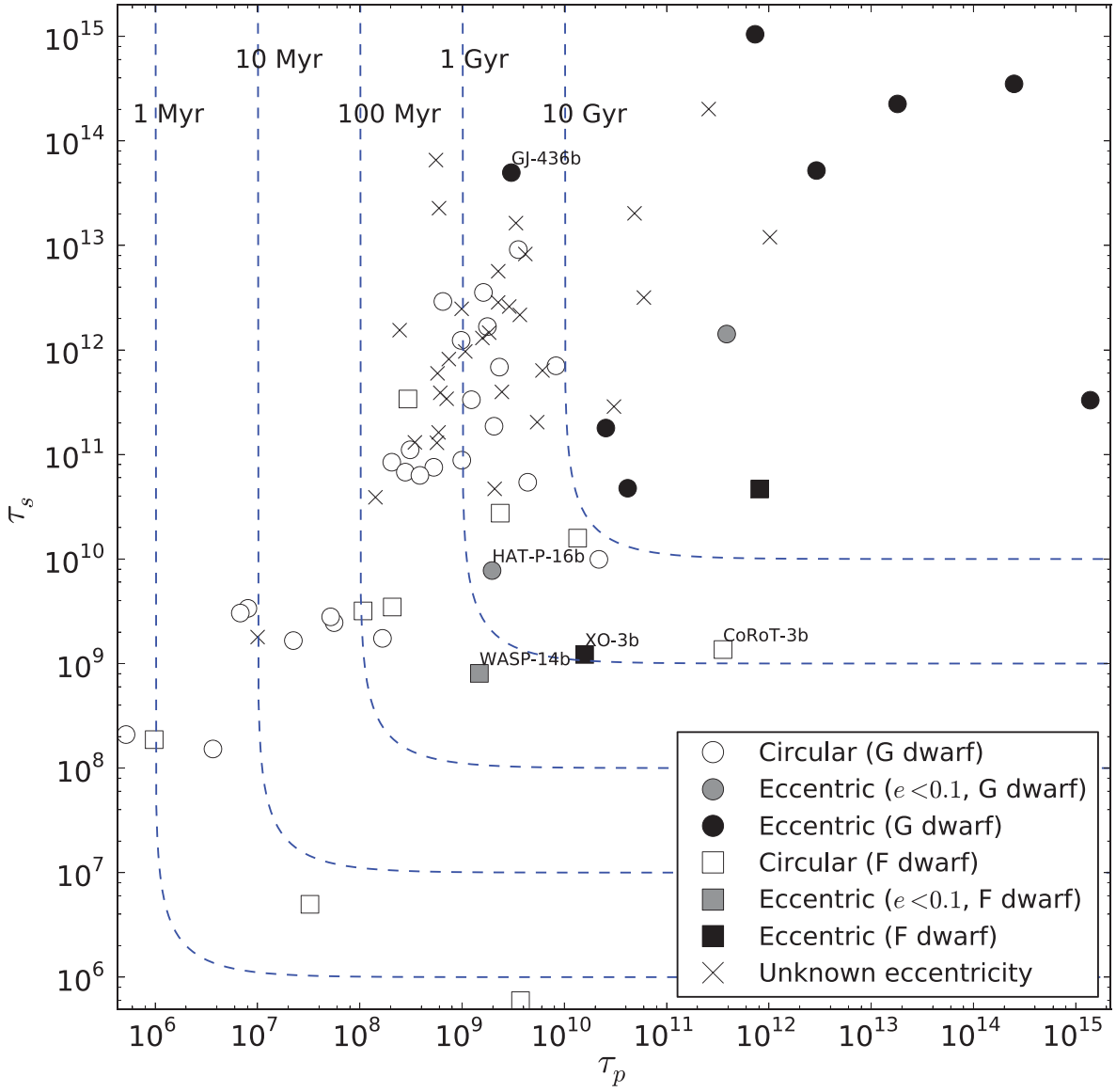

Figure 16. Plot showing the time-scale of circularization assuming tides inside the star alone (vertical axis) against the time-scale of circularization assuming tides in the planet alone (horizontal axis). The dotted lines represent lines of constant circularization time-scale. For the G dwarfs (circles), orbits that are consistent with circular and eccentric orbits are cleanly segregated by the 10 Gyr isochrone, with HAT-P-16b ($e = 0.034 \pm 0.003$) caught in the process of circularization. For the F dwarfs (squares), WASP-14b has a small eccentricity $e = 0.008 \pm 0.003$ and XO-3b has an eccentricity of 0.287 ± 0.005, whereas CoRoT-3b is on an orbit that is consistent with circular. The short time-scale for tides in the star, coupled with the relatively small eccentricities of WASP-14 and XO-3, suggests that tidal effects in the star are still operating.

in orbital eccentricity. We can therefore write

$$\tau_{\rm s} = -\left(\frac{1}{e}\frac{{\rm d}e}{{\rm d}t}\right)^{-1} = \frac{2}{21G}\frac{1}{k_{2,{\rm s}}\Delta t_{\rm s}}\frac{M_{\rm s}}{M_{\rm p}^2}\frac{a^8}{R_{\rm s}^5}. \quad (15)$$

We take some typical values of $k_{2,{\rm p}}\Delta t_{\rm p} \sim 0.01$ s and $k_{2,{\rm s}}\Delta t_{\rm s} \sim 1$ s, which would correspond to tidal quality factors (Goldreich & Soter 1966) of about 10^6 and 10^4, respectively, in the constant-Q model (in contrast to the constant Δt model that we consider here) for an orbital period of about 5 d.

We expect planets that are further out to be only weak affected by tides, whereas close-in planets will experience strong tides. Some of these close-in planets will be heavy enough and close enough to exert their own influence on the star by raising stellar tides. This can be seen in Fig. 16, where we have plotted the time-scale of circularization assuming tides inside the star alone against the time-scale of circularization assuming tides in the planet alone. The open symbols represent orbits that are consistent with circular, and the black symbols represent eccentric orbits, whereas the grey symbols represent objects with small ($e < 0.1$), but significant eccentricities. The dashed lines represent lines of constant circularization time-scale, at 1 Myr, 10 Myr, 100 Myr, 1 Gyr and 10 Gyr. For the G dwarfs, orbits that are consistent with circular and eccentric orbits are cleanly segregated by the 10 Gyr isochrone, with HAT-P-16b ($e = 0.034 \pm 0.003$) caught in the process of circularization. For the

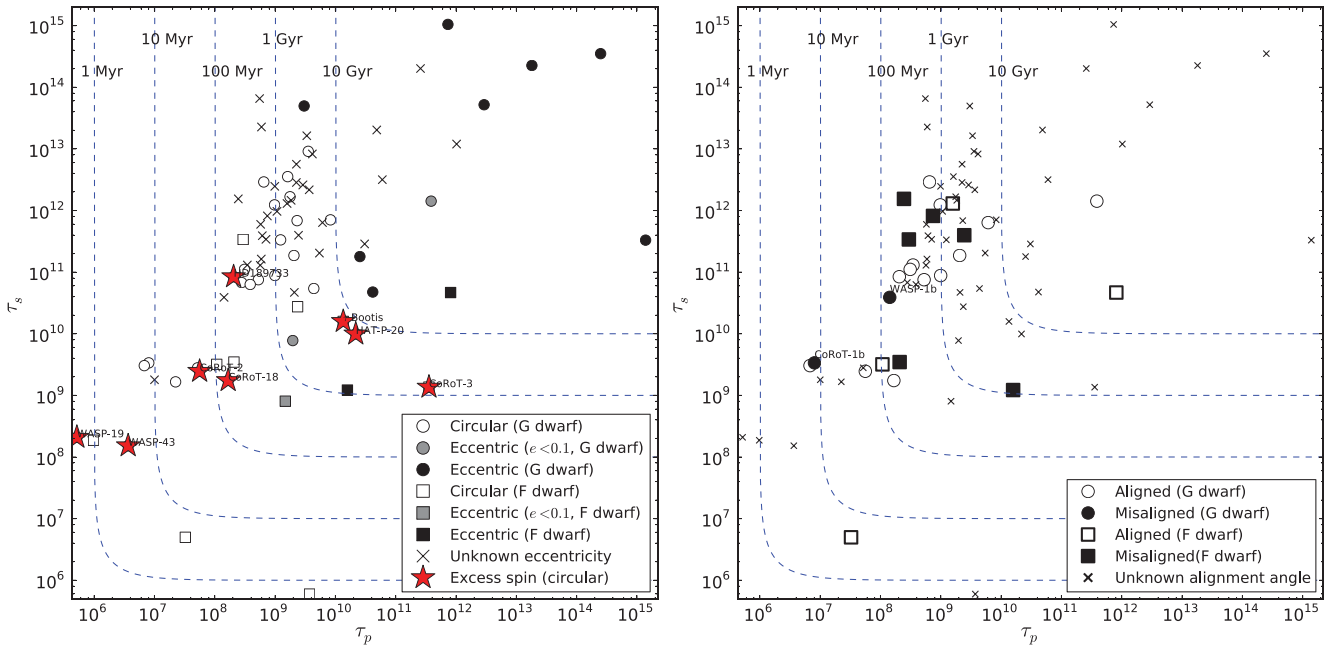

Figure 17. The axes are the same as Fig. 16. Left: the star symbols represent objects where there is evidence of spin-up. These are stars that rotate faster than predicted by the isochrones of Strassmeier & Hall (1988). In the case of the two hot stars CoRoT-3 and τ Boötis b, the stellar rotation has even become synchronized with the orbital period. No objects with a stellar tidal dissipation time-scale larger than about $\tau_s > 10^{11}$ yr show any evidence of excess rotation, supporting the case for tidal involvement in the objects with excess rotation. Right: the circles indicate aligned systems ($\lambda < 30^\circ$), whereas the star symbols represent misaligned systems ($\lambda > 30^\circ$). In this case, the G dwarfs are aligned (CoRoT-1 and WASP-1 are actually hot stars, and WASP-8 is outside the region of strong tides in the star). The F dwarfs, on the other hand, display a spread in terms of aligned and misaligned, even in cases of strong tides, in agreement with Winn et al. (2010).

F dwarfs (open symbols), WASP-14b ($T_{\rm eff} = 6475 \pm 100$ K) has a small eccentricity $e = 0.008 \pm 0.003$ and XO-3b ($T_{\rm eff} = 6429 \pm 100$ K) has an eccentricity of 0.287 ± 0.005, whereas CoRoT-3b ($T_{\rm eff} = 6740 \pm 140$ K) is on an orbit that is consistent with circular. This suggests that the dissipation factor in hotter stars may vary in an unknown fashion, although the small eccentricity of WASP-14b and the moderately small eccentricity of XO-3, together with the short time-scale for stellar tides, indicate that tides in the star are clearly important even in these cases.

5.3 Hot Neptunes

GJ-436b is a planet on an eccentric orbit ($e = 0.153 \pm 0.017$) in a region of the mass-scale plane where tidal effects on the planet are expected to be significant. The planet is a hot Neptune so it is possible that the structure is different enough that the tidal quality factor Q is very much higher, leading to a longer circularization time-scale. In this case, GJ-436b would simply not have had enough time to circularize its orbit. Another possibility that was initially suggested by Maness et al. (2007) is that a second companion may be present in the system and is pumping up the eccentricity of GJ-436b by secular interactions. Further measurements with RV (Ribas et al. 2009) and photometry (Ballard et al. 2010) appear to rule this possibility out.

5.4 Synchronization

Tidal dissipation leading to orbital circularization can occur in either the planet, the star or both, according to the time-scale for each case. On the other hand, synchronization of the host star rotation with the orbital motion would depend on tidal effects inside the star alone. This would occur on a similar time-scale as circularization in the case of dissipation in the star alone. Fig. 17 shows the same axes as Fig. 16, but on the left panel, the red star symbols represent objects with excess stellar rotation. In the case of CoRoT-3b and τ Boötis b, the rotation of the host star has been synchronized with the orbital period. Pont (2009) also pointed out that HD 189733 and CoRoT-2b were rotating faster than expected from the isochrones of Strassmeier & Hall (1988), even if the stellar rotations were not synchronized. We can now confirm that four more objects are clearly in this regime: CoRoT-18, HAT-P-20, WASP-19 and WASP-43. The rotation periods of these stars and the expected rotation periods are shown in Table 20. From Fig. 17, we note that the estimated time-scale for orbital circularization due to tidal effects in the star alone is less than 5 Gyr for the objects WASP-19, WASP-43, CoRoT-2,

Table 20. Displayed are the systems with excess rotation in the left-hand panel of Fig. 17. $P_{\rm rot}$ is the stellar rotation period today, and 'Expected $P_{\rm rot}$' is the expected rotation period of the star as estimated from the rotation isochrones of Strassmeier & Hall (1988).

Name	$P_{\rm rot}$ (d)	Expected $P_{\rm rot}$ (d)
CoRoT-2	4.52 ± 0.02	36
CoRoT-18	6.3 ± 0.9	49
HAT-P-20	11.3 ± 2.2	57
HD 189733	12.95 ± 0.01	57
WASP-19	10.5 ± 0.2	42
WASP-43	7.6 ± 0.7	57

CoRoT-18 and CoRoT-3. This means that tidal dissipation in the star could lead to the excess rotation well within the lifetime of these stars. On the other hand, the two objects τ Boötis b and HAT-P-20 have time-scales $\tau_s \sim 10$ Gyr, while HD 189733b has $\tau_s \sim 80$ Gyr. Even in this case, it should be noted that the tidal dissipation strength would have to be stronger by a single order of magnitude for these objects to have been spun up by tidal dissipation inside the star. Given that the tidal time lag is uncertain by up to about two orders of magnitude, this does not sound implausible. In contrast, orbital circularization in many of these cases may well have occurred due to dissipation in the planet instead. Planets that are unable to spin-up their parent stars to synchronization may be doomed to destruction. Hellier et al. (2009b) pointed out that the existence of WASP-18 at its current position in the mass–period plane suggests that either the tidal dissipation in the system is several orders of magnitude smaller than expected, or the system is caught at a very special time while it is in the last 10^{-4} of the estimated lifetime of the system. The latter possibility sounds more plausible, considering the striking paucity of heavy planets at short period.

5.5 Spin–orbit alignment

The right-hand panel of Fig. 17 shows the same axes (time-scales), but now the circles represent G stars and the squares represent F stars. The empty symbols represent aligned systems ($\lambda < 30^\circ$), and the filled symbols represent misaligned systems ($\lambda > 30^\circ$). In this case, the G dwarfs are aligned, except for CoRoT-1($T_{\rm eff} = 5950 \pm 150$ K) and WASP-1 ($T_{\rm eff} = 6110 \pm 245$ K) are actually hot stars, and WASP-8 is outside the region of strong tides in the star. CoRoT-1, WASP-1 and the F dwarfs display a spread in terms of aligned and misaligned, even in cases of strong tides. Winn et al. (2010) found a link between the presence of a convective envelope and spin–orbit alignment by tidal effects. Thus, exoplanets could migrate inwards by planet–planet scattering, giving rise to orbits with a range of eccentricities and spin–orbit angles. Planets in orbit around cooler stars ($T_{\rm eff} < 6250$ K, where the stellar convective region is significant) can have their orbital angular momentum aligned with the stellar rotation, while planets in orbit around hot stars ($T_{\rm eff} > 6250$ K, where the extent of the convective region is negligible) manage to keep their initial misalignment.

6 CONCLUSION

We have recalculated estimates of orbital eccentricity for a population of known transiting planets and included a noise treatment to account for systematic effects in the data. As Laughlin et al. (2005) showed using synthetic data, analysis of RV data can result in a derived eccentricity at a few σ level even in cases where the orbit is in fact consistent with circular. In a similar way, correlated noise in the instrument or atmosphere, stellar activity or additional companions to the host star can cause a spurious eccentricity detection, the cases of WASP-12 and WASP-10 being two examples highlighted in this paper.

Once these confusing effects are accounted for, a much clearer picture emerges, highlighting the importance of tidal interactions in close-in exoplanet systems. The present observations support a scenario where low-mass hot Jupiters migrate inwards and circularize their orbits until they stop at a minimum period for a given mass, conglomerating on the mass–period relation of Mazeh et al. (2005). The heavier planets are able to move further inwards before they stop. Planets heavier than about 1.2 M_j can raise tides on the star as they migrate inwards, leading to a spin-up of the host star (Pont 2009), and even spin–orbit synchronization in some cases where enough angular momentum can be transferred from the orbital motion into the stellar rotation. This appears to be the case for CoRoT-3b, τ Boötis b, HD 189733, CoRoT-2b, CoRoT-18, HAT-P-20, WASP-19 and WASP-43, where the first two are synchronized, and the rest show clear evidence of excess rotational angular momentum in the star. If the planetary angular momentum is insufficient, the process can lead to a run-away migration and the planet is destroyed, as appears to be the case for WASP-18b (Hellier et al. 2009a). This is also supported by the lack of such heavy planets at short period. As suggested by Winn et al. (2010), tidal effects in G dwarfs are also responsible for aligning the spin of the star with the orbit of the planet, whereas the same effect is much less effective in the case of the hotter F stars. Overall, therefore, the present data on close-in exoplanets support the case for a prominent role for tidal interactions between the planet and the host star in the orbital evolution of hot Jupiters.

ACKNOWLEDGMENTS

We are grateful to the anonymous referee for the encouraging remarks and the enormous amount of detailed feedback and sound advice, which helped us to make this paper better. We thank the editor for his encouraging comments. FP is grateful for the STFC grant and Halliday fellowship ST/F011083/1. We also thank the SOPHIE Exoplanet Consortium for arranging a flexible observation schedule for our programme, and the whole OHP/SOPHIE team for support. NH thanks Gilles Chabrier for his clear explanations of the equilibrium tides model.

REFERENCES

Alonso R., Guillot T., Mazeh T., Aigrain S., Alapini A., Barge P., Hatzes A., Pont F., 2009a, A&A, 501, L23
Alonso R. et al., 2009b, A&A, 506, 353
Anderson D. R. et al., 2008, MNRAS, L4, 387
Anderson D. R. et al., 2010, ApJ, 709, 159
Anderson D. R. et al., 2011, MNRAS, doi:10.1111/j.1365-2966.2012.20635.x
Bakos G. Á. et al., 2011, ApJ, 742, 116
Ballard S. et al., 2010, ApJ, 716, 1047
Baraffe I., Selsis F., Chabrier G., Barman T. S., Allard F., Hauschildt P. H., Lammer H., 2004, A&A, 419, L13
Barros S. C. C. et al., 2011, A&A, 525, A54
Bonomo A. S. et al., 2010, A&A, 520, A65
Buchhave L. A. et al., 2010, ApJ, 720, 1118
Burke C. J. et al., 2007, ApJ, 671, 2115
Butler R. P., Vogt S. S., Marcy G. W., Fischer D. A., Wright J. T., Henry G. W., Laughlin G., Lissauer J. J., 2004, ApJ, 617, 580
Butler R. P. et al., 2006, ApJ, 646, 505
Campo C. J. et al., 2011, ApJ, 727, 125
Christian D. J. et al., 2009, MNRAS, 392, 1585
Collier Cameron A. et al., 2007, MNRAS, 375, 951
Deeg H. J. et al., 2010, Nat, 464, 384
Deming D., Harrington J., Laughlin G., Seager S., Navarro S. B., Bowman W. C., Horning K., 2007, ApJ, 667, L199
Fernandez J. M., Holman M. J., Winn J. N., Torres G., Shporer A., Mazeh T., Esquerdo G. A., Everett M. E., 2009, AJ, 137, 4911
Ford E. B., 2006, ApJ, 642, 505
Ford E. B., Rasio F. A., 2006, ApJ, 638, L45
Gillon M. et al., 2009a, A&A, 496, 259
Gillon M. et al., 2009b, A&A, 501, 785
Goldreich P., Soter S., 1966, Icarus, 5, 375
Hebb L. et al., 2009, ApJ, 693, 1920
Hebb L. et al., 2010, ApJ, 708, 224

Hébrard G. et al., 2008, A&A, 488, 763
Hébrard G. et al., 2010, A&A, 516, A95
Hébrard G. et al., 2011, A&A, 533, A130
Hellier C. et al., 2009a, Nat, 460, 1098
Hellier C. et al., 2009b, ApJ, 690, L89
Hellier C. et al., 2011, A&A, 535, L7
Henry G. W., Winn J. N., 2008, AJ, 135, 68
Holman M. J. et al., 2006, ApJ, 652, 1715
Howard A. W. et al., 2010, preprint (arXiv:1008.3898)
Husnoo N. et al., 2011, MNRAS, 413, 2500
Hut P., 1981, A&A, 99, 126
Johnson J. A. et al., 2011, ApJ, 735, 24
Joshi Y. C. et al., 2009, MNRAS, 392, 1532
Kipping D., Bakos G., 2011, ApJ, 730, 50
Kipping D. M. et al., 2011, AJ, 142, 95
Kovacs G. et al., 2007, ApJ, 670, L41
Kovács G. et al., 2010, ApJ, 724, 866
Lagrange A., Desort M., Galland F., Udry S., Mayor M., 2009, A&A, 495, 335
Lanza A. F. et al., 2009, A&A, 493, 193
Laughlin G., Marcy G. W., Vogt S. S., Fischer D. A., Butler R. P., 2005, ApJ, 629, L121
Leconte J., Chabrier G., Baraffe I., Levrard B., 2010, A&A, 516, A64
Liddle A. R., 2007, MNRAS, 377, L74
Loeillet B. et al., 2008, A&A, 481, 529
Maciejewski G. et al., 2011a, MNRAS, 411, 1204
Maciejewski G., Errmann R., Raetz S., Seeliger M., Spaleniak I., Neuhäuser R., 2011b, A&A, 528, A65
Maness H. L., Marcy G. W., Ford E. B., Hauschildt P. H., Shreve A. T., Basri G. B., Butler R. P., Vogt S. S., 2007, PASP, 119, 90
Mathieu R. D., Mazeh T., 1988, ApJ, 326, 256
Mazeh T., 2008, in Goupil M.-J., Zahn J.-P., eds, EAS Publications Series Vol. 29, Observational Evidence for Tidal Interaction in Close Binary Systems. Cambridge Univ. Press, Cambridge, p. 1
Mazeh T., Zucker S., Pont F., 2005, MNRAS, 356, 955
Nutzman P. et al., 2011, ApJ, 726, 3
O'Donovan F. T. et al., 2006, ApJ, 651, L61
Pál A. et al., 2008, ApJ, 680, 1450
Pepe F., Mayor M., Galland F., Naef D., Queloz D., Santos N. C., Udry S., Burnet M., 2002, A&A, 388, 632
Pont F., 2009, MNRAS, 396, 1789
Pont F., Melo C. H. F., Bouchy F., Udry S., Queloz D., Mayor M., Santos N. C., 2005a, A&A, 433, L21
Pont F., Bouchy F., Melo C., Santos N. C., Mayor M., Queloz D., Udry S., 2005b, A&A, 438, 1123
Pont F., Zucker S., Queloz D., 2006, MNRAS, 373, 231
Pont F. et al., 2009, A&A, 502, 695
Pont F., Husnoo N., Mazeh T., Fabrycky D., 2011, MNRAS, 414, 1278
Quinn S. N. et al., 2012, ApJ, 745, 80
Raetz S. et al., 2009, Astron. Nachr., 330, 459
Rasio F. A., Ford E. B., 1996, Sci, 274, 954
Rauer H. et al., 2009, A&A, 506, 281
Ribas I., Font-Ribera A., Beaulieu J.-P., Morales J. C., García-Melendo E., 2009, in IAU Symp. Vol. 253, The Case for a Close-in Perturber to GJ 436 b. p. 149
Sivia D., 2006, Data Analysis: A Bayesian Tutorial. Oxford Univ. Press, Oxford
Smalley B. et al., 2011, A&A, 526, A130
Southworth J. et al., 2009, MNRAS, 396, 1023
Southworth J. et al., 2010, MNRAS, 408, 1680
Strassmeier K. G., Hall D. S., 1998, ApJS, 67, 453
Triaud A. H. M. J. et al., 2009, A&A, 506, 377
Triaud A. H. M. J. et al., 2011, A&A, 531, A24
Welsh W. F., Orosz J. A., Seager S., Fortney J. J., Jenkins J., Rowe J. F., Koch D., Borucki W. J., 2010, ApJ, 713, L145
Wilson D. M. et al., 2008, ApJ, 675, L113
Winn J. N. et al., 2005, ApJ, 631, 1215
Winn J. N., Holman M. J., Carter J. A., Torres G., Osip D. J., Beatty T., 2009a, AJ, 137, 3826
Winn J. N., Johnson J. A., Albrecht S., Howard A. W., Marcy G. W., Crossfield I. J., Holman M. J., 2009b, ApJ, 703, L99
Winn J. N., Fabrycky D., Albrecht S., Johnson J. A., 2010, ApJ, 718, L145

This paper has been typeset from a TEX/LATEX file prepared by the author.